

## Chapter 4. Numerical analysis using finite element simulation

### 4.1 Introduction to numerical analysis

Humans divide almost everything into components for the purpose of gaining a better understanding: The universe consists of enormous numbers of discrete matter, the world encompasses seven continents and four oceans, the history is told age by age and dynasty by dynasty. It is truly human nature to divide complicated things into separate, easier-to-understand, more manageable elements. This discretization process forms the basis of the finite element method.

There are eight basic steps in finite element method (FEM) [134]. In general, engineers are interested in stress and deformation in a body due to applied force, temperature distribution in a thermal problem, and fluid pressure and velocity in a fluid flow problem. These eight steps are explained below using the stress-strain problem as an example, in which displacement  $u$  is the primary concern [134].

#### Step 1. Discretization

Since it is difficult to find the distribution of the deformation, the body or domain is divided into a number of regular, smaller regions. In FEM, these small regions are called finite elements. The corners of these elements are called nodes, and the intersections between two element faces are called nodal lines. This discretization process naturally discretizes the displacement  $u$  into corresponding subdomains. The types of elements selected to be used, depending on the characteristics of the continuum, include one-dimensional beam elements, two-dimensional triangles and quadrilaterals, and three-dimensional brick elements, etc. Higher-order elements are sometimes employed to better fit the boundary shape of the body.

## Step 2. Select approximation functions

Since the displacement  $u$  is unknown at this stage, a function is selected to approximate  $u$ . Polynomials are the most common functions used because of their ease of handling. A polynomial interpolation function for  $u$  can be expressed as:

$$u = N_1u_1 + N_2u_2 + \cdots + N_mu_m \quad (\text{Eq. 4.1})$$

where  $u_1, u_2, \dots, u_m$  are the values of the unknown at the nodes,  $N_1, N_2, \dots, N_m$  are the interpolation functions, and the value of  $m$  depends on the type of elements used. For instance, first-order linear elements have  $u_1$  and  $u_2$  as unknowns or degrees of freedom.

## Step 3. Link the unknowns with the stress and strain

Define strain (gradient)-displacement (unknown) and Stress-Strain (constitutive) relationships.

## Step 4. Derive equations that will apply to the elements

These equations are often called governing equations because they describe how the elements behave. The governing equations are derived in a general term for all elements based on a principle, of which the most commonly used principles are the minimum potential energy and the minimum residual weighted residuals.

## Step 5. Assemble element equations to obtain assemblage equations

Now that the vector of unknowns for each individual element is described based on the linear relationship between the element property matrix and the vector of element nodal forces, the next step is to obtain global equations through an assembly process. This process is based on the law of compatibility or continuity, which equalizes the

displacement of the boundary nodes in adjacent elements. The global equations are then expressed by:

$$[K]\{u\} = \{U\} \quad (\text{Eq. 4.2})$$

where  $[K]$  is the assemblage property matrix,  $\{u\}$  is the assemblage vector of nodal unknowns, and  $\{U\}$  is the assemblage vector of nodal forcing parameters. Boundary conditions are also considered in this step, which leads to a modification of each of the terms in Eq. 4.2.

Step 6. Solve for the primary unknowns

The assemblage equations are a set of linear simultaneous algebraic equations that can be solved using the Gaussian elimination method. Displacements in the vector  $\{u\}$  are the primary unknowns. For a thermal problem, the primary unknown is the temperature, and for a fluid flow problem, the primary unknown is the velocity potential.

Step 7. Solve for secondary quantities

In a stress-deformation problem, the secondary quantities that can be calculated from the primary unknowns, the displacements  $u$ , are the strains, stresses, moments, etc.

Step 8. Interpretation of results

Advantages of the FEM are:

1. The properties of each element are evaluated separately. This enables the assignment of different material properties for each element. Therefore, the incorporation of any degree of inhomogeneity is essentially unrestricted [134]. Similarly, arbitrary geometry, material response, and boundary conditions can also be easily captured with no general restrictions. Any of the above nonlinearities can be intimidating, if not impossible, for an effort that seeks a theoretical solution.

2. The methodology for solving one class of problems can often be used for other classes of problems. For example, one-dimensional stress deformation, flow, and time-dependent flow of heat or fluids can be solved with very similar codes [134].
3. When supplemented by experimental tests, FEM simulation allows failure-mode assessment, material selection, and design optimization [80].

#### **4.2 Capabilities and challenges of modern finite element modeling approach**

Modern FEM technology has enormous impacts in almost every engineering field: aerospace, automobile, electronics, civil engineering... Especially when the computer industry has blurred the difference between the personal computer and the workstation and writes more user-friendly FEM codes, more and more engineers are able to run an FEM model for a quick-and-dirty simulation. Being able to define and solve an FEM is no longer the privilege of the few people who understand a lot of math.

However, the FEM is still an approximation to engineering theory. Therefore, there is only the problem of how to estimate and minimize the error rather than to find the exact answer, or even give the exact estimate of error. Table 4.1 summarizes what FEM can and cannot do (part of this table is based on email discussion [135]).

#### **4.3 Existing solder joint fatigue life prediction models**

Generally, engineers face two sets of problems. In the first scenario, the fatigue test data for an existing product are given. The challenge is to look for an appropriate fatigue model(s) to best interpret the data. The second scenario requires engineers to find the fatigue reliability of a new product, including design of testing methods, adopting failure models, and performing finite element analysis to predict reliability [136].

A good review on fatigue models of solder joints can be found in other work [136]. The models can be classified into five categories: stress-based, plastic strain-based, creep strain-based, energy-based and damage-based. Since the most commonly used and

studied fatigue models for solder joints are strain-based and energy-based models, the discussion will focus on these two categories.

**Table 4.1 Capabilities and limitations of FEM.**

<i>Reasons why FEM result is only an approximate solution</i>		<i>What FEM cannot do</i>	<i>What FEM can do</i>
1	FEM is one of the numerical approximation to engineering problems	To give exact solutions or exact estimate of error	TEND to approach the correct answer using refined elements
2	Element stress calculations are based on shape functions of the elements and estimated loading distribution	To give an exact stress answer based on estimated loading and constraints (how well can these estimates be made?)	Use simplified loading and constraints based on users' experiences and give reasonable results
3	Scattered material properties in different references & statistical nature of material properties	To use a true material property just for the Cu piece you have in hand	Specify the material that you are going to use
4	FEM models for material properties are simplified, or materials are not fully understood	To exactly model complex material behaviors	Find out what material behavior (such as elastic, plastic or creep) is dominant for the case being studied
5	Difficulty in modeling interface	A general method to account for the effects of interfacial defects	Assume all interfaces are ideal and perfectly bonded
6	Too many approximations	To believe the stress calculation results and estimate life time	Study a few design variations and compare stress results qualitatively

### 4.3.1 Plastic strain-based models

Among the plastic strain models, the Coffin-Manson model, the Soloman model, and the Engelmaier model are widely used. Each of these models is an empirical relationship between cycles-to-failure, and analytically, numerically or experimentally determined plastic shear strain range per cycle.

#### ***-Coffin-Manson Model***

In this most famous model, the number of cycles to failure, denoted by  $N_f$ , is related to the plastic strain range per cycle,  $\Delta\varepsilon_p$ , through a power law with a fatigue ductility coefficient  $\varepsilon_f'$  and a fatigue ductility exponent  $c$ , as shown in Eq. 4.3 [137]:

$$\frac{\Delta \varepsilon_p}{2} = \varepsilon'_f (2N_f)^c \quad (\text{Eq. 4.3})$$

where  $c$  is in the range of  $-0.5 \sim -0.7$ . This relationship only applies to the case in which damage is caused strictly by plastic deformation. In order to include the damage from elastic deformation, Basquin's equation is usually combined with the Coffin-Manson equation to form the "total strain equation," as shown in Eq. 4.4 [137]:

$$\frac{\Delta \varepsilon}{2} = \frac{\sigma'_f}{E} (2N_f)^b + \varepsilon'_f (2N_f)^c \quad (\text{Eq. 4.4})$$

where  $\Delta \varepsilon$  is the strain range (plastic and elastic),  $\sigma'_f$  is the fatigue strength coefficient,  $E$  is the elastic modulus,  $\varepsilon'_f$  is the fatigue ductility coefficient, and  $b$  is the fatigue strength exponent (Basquin's exponent).

Although the Coffin-Manson equation is a plastic strain-based fatigue model, various modifications to this equation have been reported, and some of them, such as Hong, et al.[138], consider the fatigue damage to be caused by the combined effects of plastic and creep strain, and therefore replace the plastic strain range term in the Coffin-Manson equation with an inelastic strain range, based on a constitutive theory.

#### ***-Solomon's low-cycle fatigue model***

This model defines the following equations, as shown in Eq. 4.5 [139]:

$$\Delta \gamma_p N_p^\alpha = \theta \quad (\text{Eq. 4.5})$$

where  $\Delta \gamma_p$  is the plastic shear strain range,  $N_p$  is the number of cycles to failure,  $\theta$  is the inverse of the fatigue ductility coefficient, and  $\alpha$  is a material constant. Since for creep is not considered, the Solomon's fatigue model is limited in its use for solder joints.

#### ***-Engelmaier fatigue model***

This is a modified Coffin-Manson equation. The total number of cycles to failure is related to the total shear strain and the modified ductility exponent  $c$ , which has been

been modified to include temperature and cycling frequency  $f$ , as shown in Eq. 4.6 [140,141]:

$$N_f = \frac{1}{2} \left( \frac{2\varepsilon_f'}{\Delta\gamma_t} \right)^{-\frac{1}{c}} \quad (\text{Eq. 4.6})$$

where  $c = -0.442 - 6 \times 10^{-4} \bar{T}_s + 1.74 \times 10^{-2} \ln(1 + f)$ ,  $\Delta\gamma_t$  is the total plastic shear strain range,  $\bar{T}_s$  is the mean cyclic solder joint temperature in °C, and  $f$  is the cyclic frequency in cycles/day. The fatigue ductility coefficient  $\varepsilon_f' \approx 0.325$  for eutectic tin-lead solder. In order to include creep damage,  $\Delta\gamma_t$  was later modified to become  $\Delta D$ , the cyclic fatigue damage term that is based on the total potential damage of creep and plastic relaxation. The applicable packages for this model include leaded and leadless TSOP package.

#### ***-Norris and Landzberg model***

Norris and Landzberg proposed a model that relates cycle frequency  $f$  and maximum temperature  $T_{\max}$  with solder joint fatigue life [23]:

$$N_f = c \cdot f^m (\Delta\varepsilon_p)^{-n} \exp(Q/kT_{\max}) \quad (\text{Eq. 4.7})$$

where  $c$ ,  $m$ , and  $n$  are material constants,  $\Delta\varepsilon_p$  is the plastic strain range,  $Q$  is the activation energy, and  $k$  is the Boltzmann constant. This model indicates that when cycle frequency increases, the number of cycles to failure increases accordingly. This has been largely attributed to the fact that the dwell time is reduced at higher cycle frequency.

### **4.3.2 Creep strain-based models**

#### ***- Knecht and Fox model***

Theories of creep suggest that creep in the solder joint may be due to either grain boundary sliding and/or dislocation glide (matrix creep) [131]. Knecht and Fox established a simple creep fatigue model based on the matrix creep, as shown in Eq. 4.8 [142]:

$$N_f = \frac{C}{\Delta\gamma_{mc}} \quad (\text{Eq. 4.8})$$

where  $N_f$  is the number of cycles to failure,  $\Delta\gamma_{mc}$  is the matrix creep strain range, and C is the material constant related to microstructure.

#### **- Syed model**

This model, shown in Eq. 4.9, incorporates both matrix creep and grain boundary sliding creep [143, 144]:

$$N_f = ([0.022D_{gbs}] + [0.063D_{mc}])^{-1} \quad (\text{Eq. 4.9})$$

where  $D_{gbs}$  and  $D_{mc}$  are the accumulated equivalent creep strain range for grain boundary sliding and the matrix creep, respectively. The Syed model assumes that creep is the dominant damage mechanism, and the plastic-strain effects are neglected. It is apparent that both the Knecht and Fox model and the Syed model omit plastic-strain effects, thus their use for solder joints in electronics components are limited.

### **4.3.3 Energy-based models**

In this class of fatigue life models, the fatigue failure is predicted from a hysteresis energy term or volume-weighted average stress-strain history. FEM is often used to determine the strain energy or strain energy density per cycle, although sometimes experimental stress-strain measurements are conducted.

#### **- Akay model**

The mean cycle to failure,  $N_f$ , is related to the total strain energy  $\Delta\bar{W}_{total}$  through material constants  $W_0$  and k, as shown Eq. 4.10 [145]:

$$N_f = \left(\frac{\Delta\bar{W}_{total}}{W_0}\right)^{\frac{1}{k}} \quad (\text{Eq. 4.10})$$

It is necessary to point out that this equation only gives a prediction of the number of cycles to crack initiation.

#### **- Darveaux model**

Darveaux derived a relation between the volume-weighted average plastic work density accumulated per cycle,  $\Delta W_{avg}$ , and the number of cycles to crack initiation,  $N_0$ , and the crack propagation rate,  $da / dN$ , as shown in Eq. 4.11 and Eq. 4.12 [146], respectively:

$$N_0 = C_3 \Delta W_{avg}^{C_4} \quad (\text{Eq. 4.11})$$

$$\frac{da}{dN} = C_5 \Delta W_{avg}^{C_6} \quad (\text{Eq. 4.12})$$

where  $C_3, C_4, C_5$  and  $C_6$  are crack-growth constants and  $a$  is the characteristic crack length. These constants for solder joints in thin, small-outline package (TSOP) were given as: 54.2, -1.0,  $3.49 \times 10^{-7}$ , and 1.13, respectively [147]. Gustafsson [148,149] has further developed the Darveaux model to account for primary and secondary cracks that propagate towards each other at different rates.

Advantages of the energy-based models are the inclusion of hysteresis information to fatigue modeling and thus an ability to predict the time required to accumulate sufficient energy for a crack to initiate. These models capture the test conditions better than the strain-based models.

#### **4.4 Documented FEM analysis of area array packages**

This section reviews previous work on area array solder joint reliability. To begin with, finite element work on the reliability of CBGA packages by Hong, using thermomechanical FEM analysis, is introduced, followed by a review of the numerical analysis of Ceramic Column Grid Array (CCGA) by the same author. Next, a reliability-enhanced S3 chip scale package and various solder joints including CCB/SST are introduced, and FEM modeling of these two types of packages is reviewed. In order to

evaluate the effects of underfill material on solder joint reliability, related previous numerical work is also presented.

#### 4.4.1 FEM analysis of CBGA and CCGA by IBM

The CBGA package is a surface-mounted second-level assembly that redistributes signals from one or more silicon chips, through a multilayer ceramic substrate, to the printed circuit cards by the solder joints. The first-level interconnect method could be C4 solder joints or wire bonds. Since ceramic substrate closely matches the CTE of the silicon, C4 reliability is normally not a concern. However, due to large CTE mismatch between the ceramic package and the PCB, the CBGA solder joints are widely studied for reliability improvement.

Figure 4.1 shows a C4/CBGA assembly [150]. A silicon die is connected to a multilayer ceramic substrate using C4 solder bumps. The ceramic substrate serves as a carrier, and more importantly, it routes the smaller C4 pad to an array of larger solder pads for the convenience of board-mounting. The second-level interconnection of the CBGA package is the BGA, consisting of a number of solder bumps formed using eutectic solder fillets and high-lead solder balls. The CBGA package is mounted to the PCB using eutectic solder.

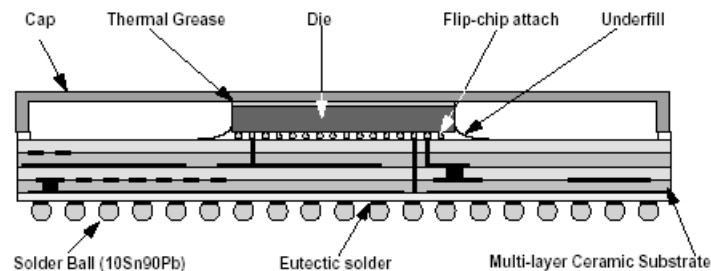


**Figure 4.1 Schematic of a C4/CBGA assembly.**

Hong, et al. [151] studied the reliability performance of a 32x32x3mm single-chip module (SCM) CBGA package that uses lead-based and lead-free solder fillets. Numerical simulation on viscoplastic deformation and thermal fatigue life of the solder fillets are examined. Three lead-free solder alloys, the antimony-tin (Sb5-Sn95), silver-tin

(ag3.5-Sn96.5), and eutectic zinc-tin (Zn9-Sn91) were considered. An FEM model of a slice of CBGA package is shown in Figure 4.2 [151].

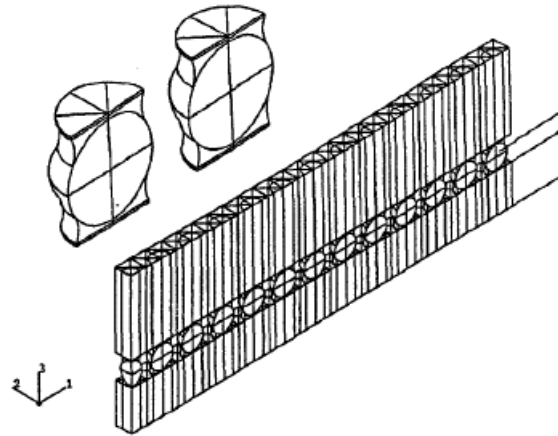


**Figure 4.2 Finite element models of the CBGA.**

The authors used a constitutive theory to account for the elastic, the plastic, the creep, and the thermal strain of the solder. The Garofalo hyperbolic sine law was used to describe the steady-state behavior. Figure 4.3 shows the equivalent inelastic strain IEEQ (sum of equivalent plastic and creep strain) of various solder fillets [151]. At an imposed cycling condition of 0°C-100 °C, two cycles/hour, the eutectic Pb-Sn solder shows the highest IEEQ. A reliability projection of these solder fillets was calculated by a modified Coffin-Manson equation using the IEEQ value. The conclusion was that the lead-free solder improves CBGA solder joint reliability by 1.69X (Sb5-Sn95), 2.62X (Ag3.5-Sn96.5), and 3.01X (Zn9-Sn91), respectively.

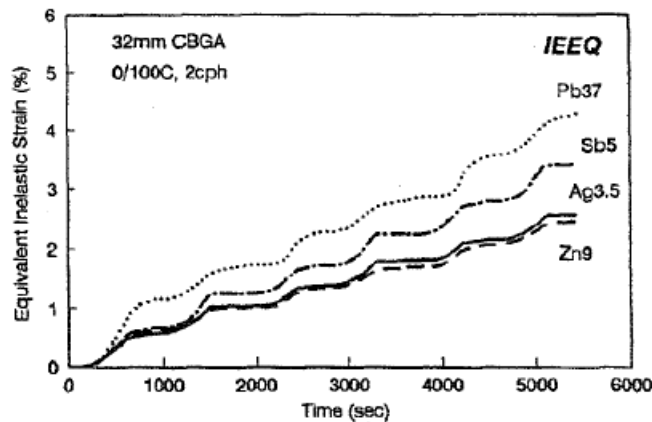


**Figure 4.3 Equivalent inelastic strain of various solder fillets.**

Hong, et al. [152] also numerically studied the reliability of IBM's CCGA assembly with Cn-Sn-coated solder columns using a similar methodology. Figure 4.4 shows the FEM model of a quarter of the assembly and details of the corner solder column. Only a single solder column that has the largest distance from neutral point (DNP) is modeled. FEM results suggested that in this case, highest strain concentration occurs at the interface between the fillet and the solder column body (A~D). An environmental test showed that cracks are indeed mostly seen at these locations. This study also showed that for the Pb90-Sn10 solder column, between the two competitive damage mechanisms, the creep is 10x more pronounced than the plastic strain.

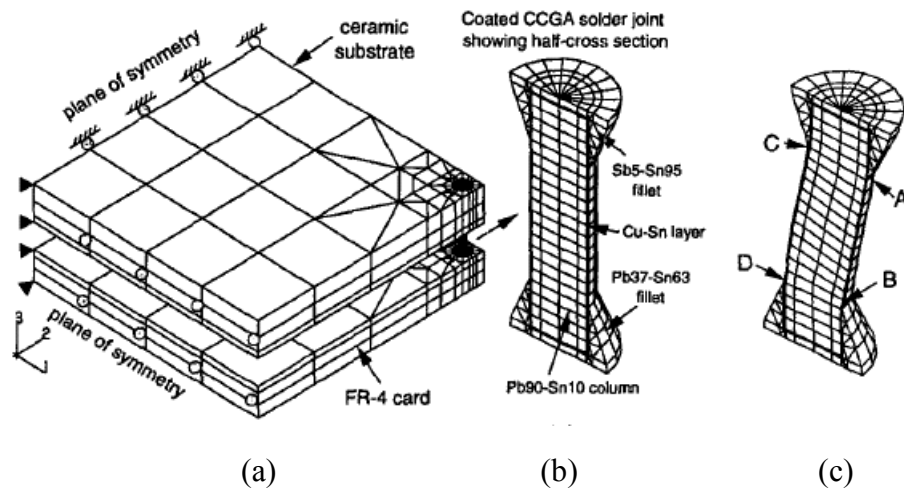


**Figure 4.4 Finite element model of CCGA assembly: (a) overall model; (b) a solder column; and (c) a deformed solder column.**

#### 4.4.2 FEM modeling of enhanced standoff height solder joints

##### *-Chip scale package S3*

Rzepka, et al. performed 2D plain-strain FEM simulation on a wafer-level chip scale package (WLCSP) of the S<sup>3</sup> structure, which employs a unique polymer-supporting process to fabricate stacked-solder balls [80]. The FEM model is shown in Figure 4.5. A good point is made in this paper by parametrically studying material stiffness factors. For each set of material Young's modulus, a critical damage path is identified using the

largest equivalent inelastic strain. With changes in epoxy stiffness, the critical path shifts from solder/chip interface to solder neck. The reason is that when a soft material is replaced with a hard epoxy, the deformation at the solder/chip interface is reduced. However, if the support structure is too hard, the chip-side solder balls are no longer adequately involved in helping to alleviate the mismatch between the package and the board. Therefore, there exists an optimum value of Young's modulus of the epoxy, which is about 5 GPa.

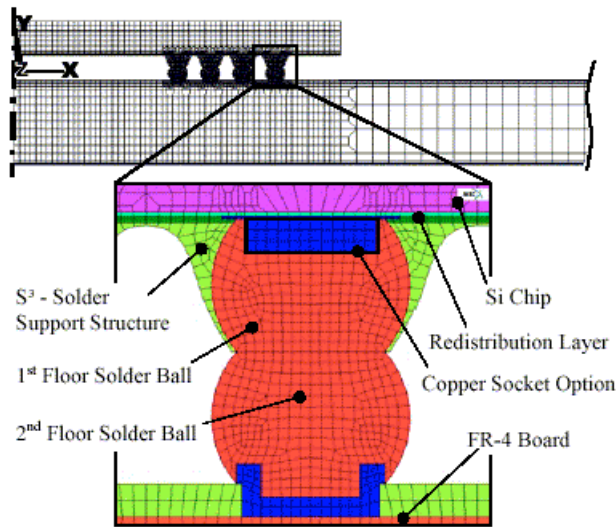


**Figure 4.5 FEM mesh of a WLCSP with stacked balls.**

Figure 4.6 shows the modeling results for the effects of underfill material [80]. It shows that the use of soft underfill does not sufficiently reduce the strain level. The hard underfill is the most effective means for the WLCSP and flip chip modules. The CTE of this material should match that of the solder, and the T<sub>g</sub> should be above the maximum processing temperature. When the operation temperature exceeds the glass transition temperature of the underfill, Young's modulus becomes much lower and the CTE mismatch shoots up. The results show that when the T<sub>g</sub> is shifted down to 90°C, most of the benefits of the hard underfill are gone.

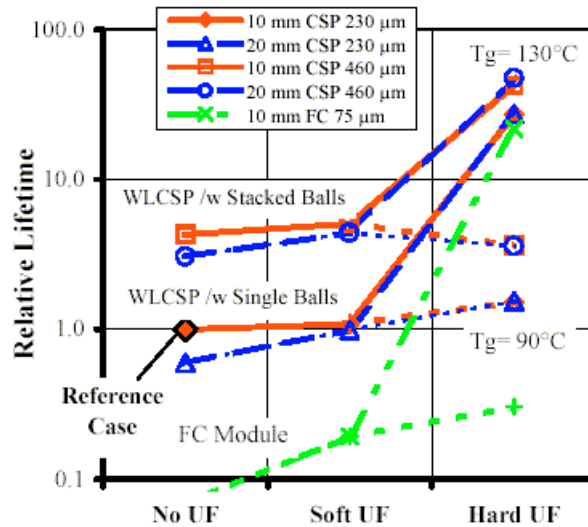
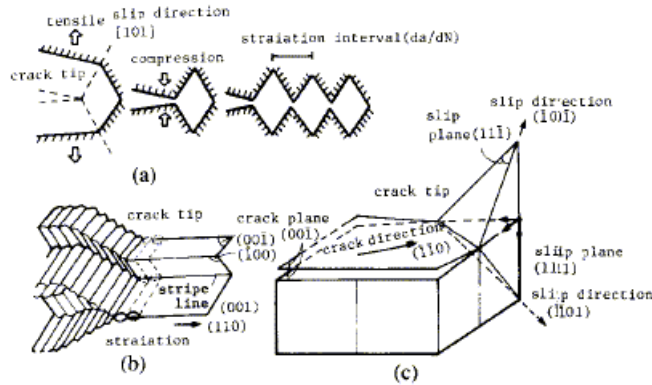


Figure 4.6 Lifetime prediction for various WLCSP and flip chip designs.

- CCB/SST

Satoh, et al. studied the thermal fatigue of Pb-Sn alloy interconnections on the CCB package, the small-outline plastic (SOP) package, and the quad flat package (QFP) [49]. This research first analyzed in detail the thermal fatigue fracture of Pb-Sn solder joints. Due to the availability of the low-acceleration-voltage (1-5 kV) field emission-scanning electron microscope (FE-SEM), observation of solder joint striations down to 0.05 μm was possible. Experiments found that striations in thermal-cycled CCB joints were about 0.15 μm and gradually became larger away from the joint edge. The number of striations roughly agreed with the number of temperature cycles. Figure 4.7 shows a schematic of the suspected thermal fatigue fracture mechanisms of the Pb-Sn5 alloy [49]. During thermal cycling, alternating tensile and compression force on a crack tip causes intergranular sliding to occur on many equivalent slip planes  $\{1\ 1\ 1\}$ . Therefore, the damage is not caused by the ordinary plastic shear or principal strain range, **rather it is caused by the equivalent strain range**, which is the von Mises yield criterion under the multiaxial stress-strain condition.



**Figure 4.7 Schematic of the thermal fatigue fracture mechanism in the Pb-5Sn alloy: (a) formation mechanism of Laird-type striation; (b) formation mechanism of the Pb alloy striation; and (c) estimation of the direction of crack propagation and slip plane.**

In order to generate a master curve for the reliability of the tested packages, three-dimensional FEM models were used to obtain strain range  $\Delta\epsilon_p$  for the CCB and the SST solder joints. Figure 4.8 shows the relationship between reliability life (tested data) and the maximum equivalent strain [49].

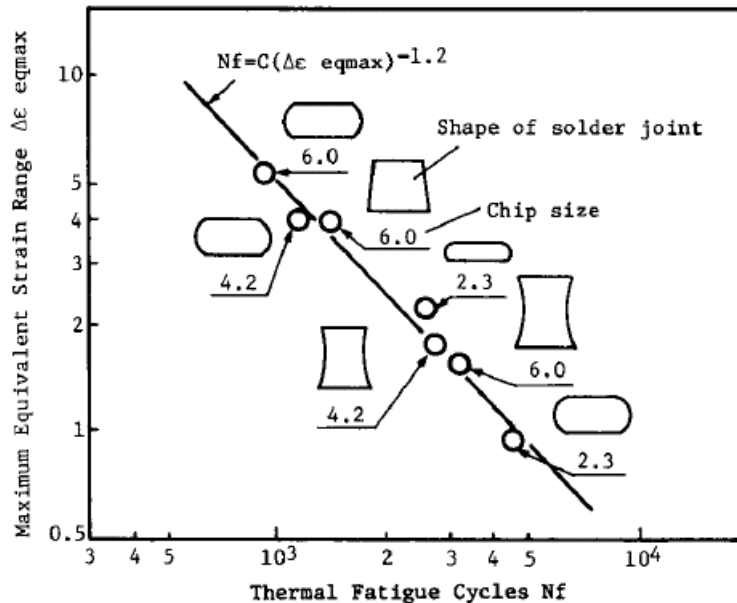


**Figure 4.8 Thermal fatigue life of CCB microsolder joints.**

#### 4.4.3 FEM modeling of underfill effects

Chen, et al. [83] studied the effects of underfill material on the reliability of flip chip packages using finite element analysis. The viscoplastic property of Sn60-Pb40 solder is considered in the simulation. 2D FEM results show that much larger strains occur at the solder/chip interface in the case of no underfill than in underfilled packages. Simulated shear stress/strain hysteresis loops indicate that high stress occurs at low temperatures, and low stresses occur at high temperatures, and that both stress relaxation and plastic flow (creep) occur simultaneously during the  $-55^{\circ}\text{C}$  and  $125^{\circ}\text{C}$  dwells. Figure 4.9 shows the deformation of the package at  $125^{\circ}\text{C}$  dwell time for packages with and without underfill [83]. The authors concluded that the reliability enhancement of underfill is due to the change of deformation mode from shear-dominated in the case without underfill to more uniform strain with package warpage for underfilled packages.

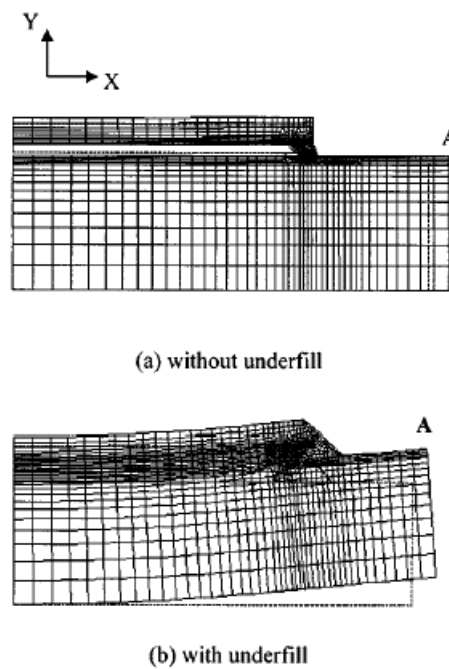


Figure 4.9 Package deformation at  $125^{\circ}\text{C}$  without (a) and with (b) underfill.

## 4.5 FEM modeling of the thermal fatigue of DAI and CCB solder joints

To correlate FEM modeling with reliability testing of the DAI and CCB samples, two cases have been studied using FEA modeling: power cycling conditions and temperature cycling conditions. The modeling process can be divided into the following seven steps:

1. Extract dimensions from real test samples.
2. Construct 3D CAD model representation.
3. Select appropriate element types and conduct meshing.
4. Select constitutive material models and incorporate into a software database.
5. Specify boundary conditions, temperature loading and convergence criteria.
6. Solve models.
7. Retrieve and interpret results.

### 4.5.1 Material models

In FEA, mechanical behavior of materials is incorporated into the finite element scheme using a constitutive model that accounts for the elastic, plastic, and viscoplastic (creep) behaviors. Each individual component of the constitutive model is based on experimental data obtained from standard bulk samples, such as the cast, dogbone-shaped specimens with rectangular cross-sections. Of course, it is definitely of great importance to study the effects of the micro-structure of the solder joint as well as the scalability of the bulk test sample data. However, so far these factors cannot be effectively considered in general FEA.

#### 4.5.1.1 Elastic model

Many metal materials, including solder alloys, exhibit an elastic response only at a low strain level. Basquin's equation [153] is widely used to relate high-cycle (low-strain) fatigue with the number of load reversals to failure  $2N_f$ :

$$\frac{\Delta \varepsilon_e}{2} = \frac{\sigma_f'}{E} (2N_f)^b \quad (\text{Eq. 4.13})$$

where  $\Delta\varepsilon_e$  is the elastic strain range,  $\sigma'_f$  is the fatigue strength coefficient defined by the stress intercept at  $2N_f = 1$ , E is the elastic modulus, and b is the fatigue strength exponent (Basquin's exponent). A smaller value of b results in a longer fatigue life. Figure 4.10 shows the fatigue strain-life curve obtained by superposition of elastic and plastic strain-life equations [136]. Since ductile materials give the best fit for high-cyclic-strain conditions, while strong materials give the best results for low-strain situations [154], elastic low-strain fatigue is not as pronounced as the plastic high-strain fatigue in solder.

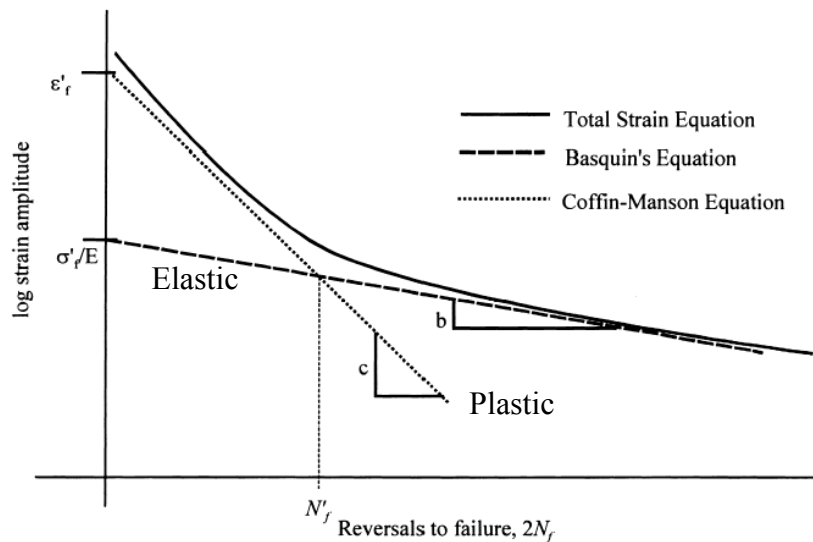


**Figure 4.10 Total strain versus life equation (reprinted with permission of L. T. Nguyen).**

#### 4.5.1.2 Plastic models

Classical plasticity models contain three fundamental ingredients [155,156]:

1. A yield function or yield criterion defines the limit of elastic behavior for a general state of stress.
2. A flow rule determines the relative magnitudes of the components of the plastic strain increment tensor.
3. A hardening rule defines the changes in the yield function as a result of plastic straining.

The yield function may be thought of as a closed surface in a six-dimensional stress space. It divides the stress space into two regions. Points inside the yield surface are characterized by elastic stress-strain behavior, while stress states on the yield surface are at the limit of elastic behavior. The yield function  $F$  may be written as a function of stress and a hardening parameter  $k$ , as in Eq. 4.14:

$$F(\sigma_{ij}) - k = 0 \quad (\text{Eq. 4.14})$$

The most commonly used yield function is the von Mises (or distortion-energy) yield function. For an isotropic hardening material, this function is stated as:

$$F = J_2 - \frac{1}{3} \sigma_{yield}^2 \quad (\text{Eq. 4.15})$$

$$J_2 = \frac{1}{2} s_{ij} s_{ij} \quad (\text{Eq. 4.16})$$

where  $\sigma_{yield}$  is the yielding strength of the material under uniaxial tension test.  $J_2$  is the second invariant of the deviatoric stress tensor. The deviatoric stresses,  $s_{ij}$ , are given by Eq. 4.16:

$$s_{ij} = \sigma_{ij} - \sigma_m \delta_{ij} \quad (\text{Eq. 4.16})$$

where  $\sigma_{ij}$  is the stress tensor,  $\sigma_m = \frac{\sigma_x + \sigma_y + \sigma_z}{3}$  is the hydrostatic or mean stress, and  $\delta_{ij}$  is the Kronecker delta, defined by Eq. 4.17:

$$\delta_{ij} = \begin{vmatrix} 1 & 0 & 0 \\ 0 & 1 & 0 \\ 0 & 0 & 1 \end{vmatrix} = \begin{cases} 1 & i = j \\ 0 & i \neq j \end{cases} \quad (\text{Eq. 4.17})$$

The von Mises' yield criterion implies that yielding is not dependent on any particular normal stress or shear stress; rather, it depends on a function of the total stress state. Furthermore, von Mises' yield criterion implies that the yielding is independent of the hydrostatic component (responsible for volume change) of a complex state of stress;

therefore, only the deviator stresses  $s_{ij}$  (involves change in shape/distortion) accounts for the yielding [157].

Materials yielding results in plastic strain. There are two theories of plastic stress-strain relationships [157]. *Deformation* or *total strain* theories relate the stresses to the total plastic strain. *Incremental* or *flow theories* (Levy-Mises equations) relate the stresses to the plastic strain increments  $d\epsilon_{ij}^{pl}$ , with the advantages of being able to describe loading history. Levy-Mises equations state that for an ideal plastic solid, at any instant of deformation the ratio of the plastic strain incremental increases to the current deviatoric stresses is constant. The Prandtl-Reuss equations extends the flow theories to incorporate consideration of elastic strain. The total strain increment is expressed as:

$$d\epsilon_{ij} = d\epsilon_{ij}^E + d\epsilon_{ij}^{pl} \quad (\text{Eq. 4.18})$$

where  $d\epsilon_{ij}$  is the total strain,  $d\epsilon_{ij}^E$  is the elastic strain, and  $d\epsilon_{ij}^{pl}$  is the plastic strain described by the Levy-Mises equations.

The yield surface may change in size or shape and translate in the six-dimensional stress space as a result of plastic straining. These changes are computed based on the hardening rule. Common hardening rules available in the FEA software include isotropic hardening, Prager kinematic hardening, and Ziegler-Prager kinematic hardening, etc.

Isotropic hardening assumes that the yield surface expands uniformly as a result of plastic straining, while Kinematic hardening assumes that the yield surface translates in the stress space but does not change size or shape. For an isotropic hardening material, the effective von Mises stress is given by Eq. 4.19:

$$\sigma = \sqrt{3J_2} = \sqrt{\frac{3}{2}s_{ij}s_{ij}} = \sqrt{\frac{1}{2}[(\sigma_{xx} - \sigma_{yy})^2 + (\sigma_{yy} - \sigma_{zz})^2 + (\sigma_{zz} - \sigma_{xx})^2 + 6\tau_{xy}^2 + 6\tau_{yz}^2 + 6\tau_{zx}^2]} \quad (\text{Eq. 4.19})$$

In FEM software such as ABAQUS and I-DEAS, nonlinear statics analysis is based on the classical plasticity formulation with the von Mises criterion. It's the user's choice to decide the hardening rule. Isotropic hardening, although simple, does not apply to most

materials that are subjected to cycling load. Kinematic hardening rules are preferred in these analyses.

The effective or equivalent plastic strain is defined as:

$$\varepsilon^{pl} = \int_0^t d\varepsilon^{pl} dt \quad (\text{Eq. 4.20})$$

For classic metals (Mises):

$$d\varepsilon^{pl} = \sqrt{\frac{2}{3} d\varepsilon_{ij}^{pl} d\varepsilon_{ij}^{pl}} \quad (\text{Eq. 4.21})$$

Similarly, the equivalent creep strain is defined as:

$$\varepsilon^{cr} = \int_0^t d\varepsilon^{cr} dt \quad (\text{Eq. 4.22})$$

For classic metals (Mises):

$$d\varepsilon^{cr} = \sqrt{\frac{2}{3} d\varepsilon_{ij}^{cr} d\varepsilon_{ij}^{cr}} \quad (\text{Eq. 4.23})$$

#### 4.5.1.3 Creep models

Commonly used creep models include the power law and the hyperbolic sine law to describe the steady-state creep strain rate. Transient creep can also be described at constant stress and temperature conditions.

##### 1) Power law

$$\dot{\bar{\varepsilon}} = \dot{\varepsilon} \left[ \frac{\bar{\sigma}}{g(\bar{\varepsilon})} \right]^m, \quad g(\bar{\varepsilon}) = \sigma_0 \left[ \frac{\bar{\varepsilon}}{\varepsilon_0} + 1 \right]^N \quad (\text{Eq. 4.24})$$

where  $\dot{\bar{\varepsilon}}$  is the viscoplastic strain rate,  $\dot{\varepsilon}$  is a reference strain rate,  $\bar{\sigma}$  is the magnitude of  $\sigma$ ,  $m$  is the rate sensitivity exponent,  $\sigma_0$  is the yield stress,  $\varepsilon_0$  is the strain at the yield stress, and  $N$  describes hardening [158].

## 2) Hyperbolic sine law

The hyperbolic sine law, sometimes referred to as the Garofalo hyperbolic sine law, models the secondary creep (steady creep) behavior. This relationship covers the low- and high-stress regimes, as expressed by Eq. 4.25:

$$\dot{\epsilon}^{cr} = A(\sinh B\sigma)^n \exp\left(-\frac{\Delta H}{RT}\right) \quad (\text{Eq. 4.25})$$

where  $\dot{\epsilon}^{cr}$  is the uniaxial tensile creep strain rate,  $\sigma$  is the applied uniaxial tensile stress, A, B, and n are material constants,  $\Delta H$  is the apparent activation energy, R is the gas constant (8.314 J/mole-K), and T is the absolute temperature [159,154].

## 3) Transient creep at constant stress and temperature

$$\epsilon_c = \frac{d\epsilon_s}{dt} \cdot t + \epsilon_T (1 - \exp(-B \frac{d\epsilon_s}{dt} \cdot t)) \quad (\text{Eq. 4.26})$$

where  $\epsilon_c$  is the creep strain,  $\frac{d\epsilon_s}{dt}$  is the steady-state creep rate,  $\epsilon_T$  is the transient creep strain, and B is the transient creep coefficient. This equation, after taking the time derivative of both sides, indicates that at time equal to zero, the instantaneous creep rate is  $(1 + \epsilon_T B)$  times greater than the steady-state creep rate [154].

### 4.5.1.4 Thermal strains

For orthotropic materials, the CTE can be different for the three principal material axes: xx, yy and zz. The CTE with respect to the principal material axes,  $\sigma_{xx}$ ,  $\sigma_{yy}$ , and  $\sigma_{zz}$ , therefore must be defined. The following relationship applies for this type of material [155]:

$$\begin{Bmatrix} \epsilon_{xx}^{th} \\ \epsilon_{yy}^{th} \\ \epsilon_{zz}^{th} \\ \gamma_{xy}^{th} \\ \gamma_{xz}^{th} \\ \gamma_{yz}^{th} \end{Bmatrix} = \Delta T \begin{Bmatrix} \alpha_{xx} \\ \alpha_{yy} \\ \alpha_{zz} \\ 0 \\ 0 \\ 0 \end{Bmatrix} \quad (\text{Eq. 4.27})$$

where  $\Delta T$  is the temperature difference between the material temperature and the strain-free reference temperature.

#### 4.5.1.5 Material models used in this analysis

Solder materials are the most complicated part to model because of temperature- and time-dependent viscoplastic behavior. The field temperature of solder joints is in the range of 0.5~0.8  $T_m$  (melting temperature); therefore creep behavior is prominent and can not be neglected. The temperature-dependency of the plasticity of solder alloys further complicates the problem. In general, solder becomes soft (has a lower Young's modulus and yielding strength) when the temperature increases. In this investigation, a constitutive theory developed by Hong and Burrell [151] was used to model solder material. According to this theory, the total strain in the solder joint is assumed to be the sum of the elastic, the plastic, the creep, and the thermal strain. The Prandtl-Reuss equations are used to describe the elastic-plastic behavior of solder. At this time, only the steady-state creep can be modeled using ABAQUS, for which the Garofalo hyperbolic sine law was used.

Silicon is assumed to be linear elastic. Copper is modeled as kinematic hardening (with a bilinear stress-strain curve), with a yield strength of 138 MPa at  $\epsilon = 0.121\%$  and a hardening modulus of 1.35 GPa after yielding.

Material properties used in this analysis are summarized in Tables 4.2 and 4.3.

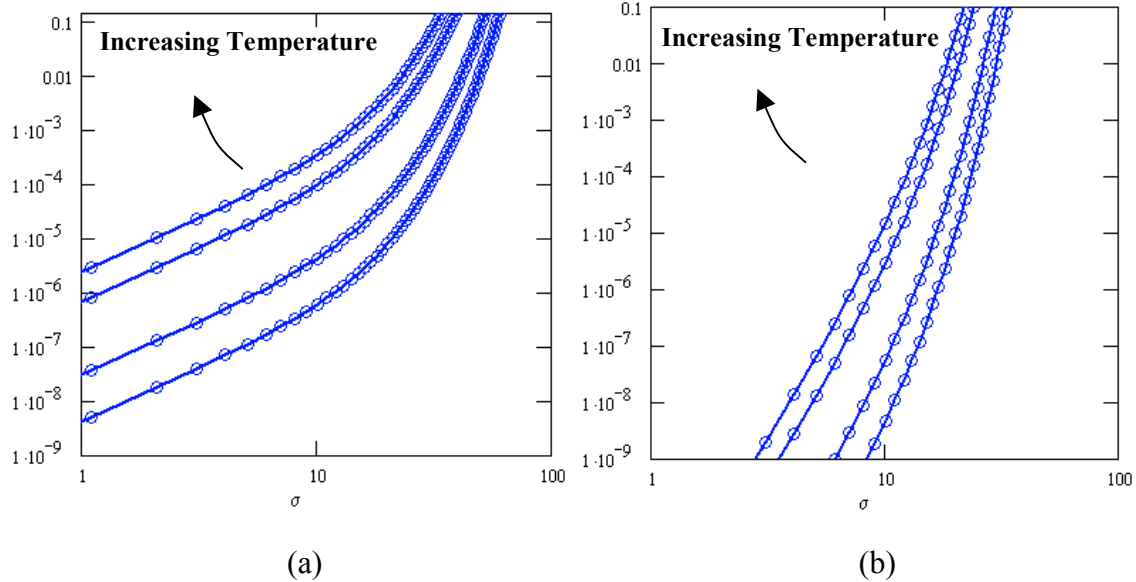
**Table 4.2 Material properties used in the FEM analysis.**

Materials		Cu	AlN	Si	63Sn37Pb		
Density	Kg/m <sup>3</sup>	8930	3260	2330	8470		
Modulus	GPa	135	330	130	26.4	12.5	6.9
Poisson ratio		0.34	0.23	0.28	.36	.365	.378
Yield strength	MPa	138			36.4	15.2	9.6
CTE	ppm/K	17	4.5	4.1	25.2	26.1	27.3
Reference Temperature	K	273	273	273	273	323	373

**Table 4.3 Visco-plastic properties of eutectic solders.**

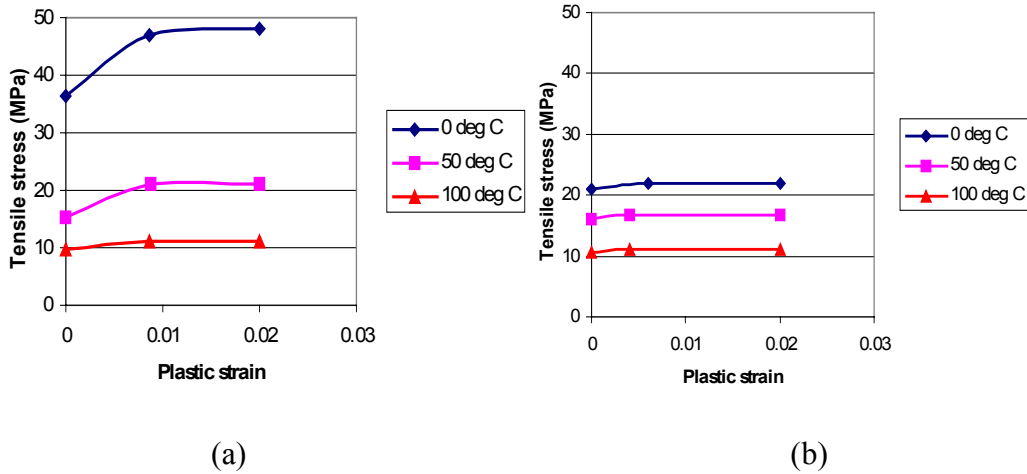
<i>Creep Constants for Hyperbolic Sine Law</i>					
Solders	A (1/sec)	B (1/Pa)	n	$\Delta H$ (J/mol)	R (J/mol·K)
Pb37-Sn63	12423	0.126E-6	1.89	61417	8.314
Ag3.5-Sn96.5	98437	0.103	6.65	79500	8.314

Figure 4.11 shows the steady-state creep strain rate of the Pb37-Sn63 solder (a) and the Ag3.5-Sn96.5 solder (b) as a function of stress at various temperatures (25°C, 50°C, 100°C and 125°C). The curves are calculated based on the hyperbolic sine law.



**Figure 4.11 Steady-state creep strain rate of the Pb37-Sn63 solder (a) and the Ag3.5-Sn96.5 solder (b) as a function of stress at various temperatures.**

The temperature-dependent plasticity of the eutectic Pb37-Sn63 solder (a) and the eutectic Ag3.5-Sn96.5 solder (b) is shown in Figure 4.12.



**Figure 4.12 Plastic properties of (a) the eutectic Pb-Sn solder and (b) the eutectic Ag-Sn solder.**

## 4.5.2 Modeling process

### 4.5.2.1 Construction of FEM models

The geometry and meshing of these models were made in MSC/PATRAN, a commercially available pre/post-processing software. The FEM models are solved in ABAQUS code using an input file generated from PATRAN. The results file from ABAQUS, including \*.odb and \*.fil files, are then read back into the PATRAN database for interpretation (.fil) or evaluated in ABAQUS/CAE (.odb), respectively.

Modeling of a dimple solder joint and copper flex is given as follows as an example of the modeling process (Figures 4.13 (a) through (d)). Meshing of the CCB solder joints is similar, but is much easier due to the flat copper interconnect.

(a) Geometry of the Dimple Array solder joint is first imported into PATRAN.

(b) In order to use the eight-node linear brick element for a better stress simulation accuracy than the four-node tetrahedral element, extrusion or revolving of four-node quad element, is required. To do this, the imported geometry, mainly the irregular surfaces, are sub-divided into smaller, three- or four-edged ones. The number of elements along each

edge (mesh seed) of these surfaces is specified to control the mesh density. Then the surfaces are meshed with four-node shell meshes.

(c) The solder joint mesh is generated by extrusion, lofting and revolving operations of the quad mesh.

(d) Similarly, the copper dimple mesh is generated using extrusion and revolving of the defined quad mesh.

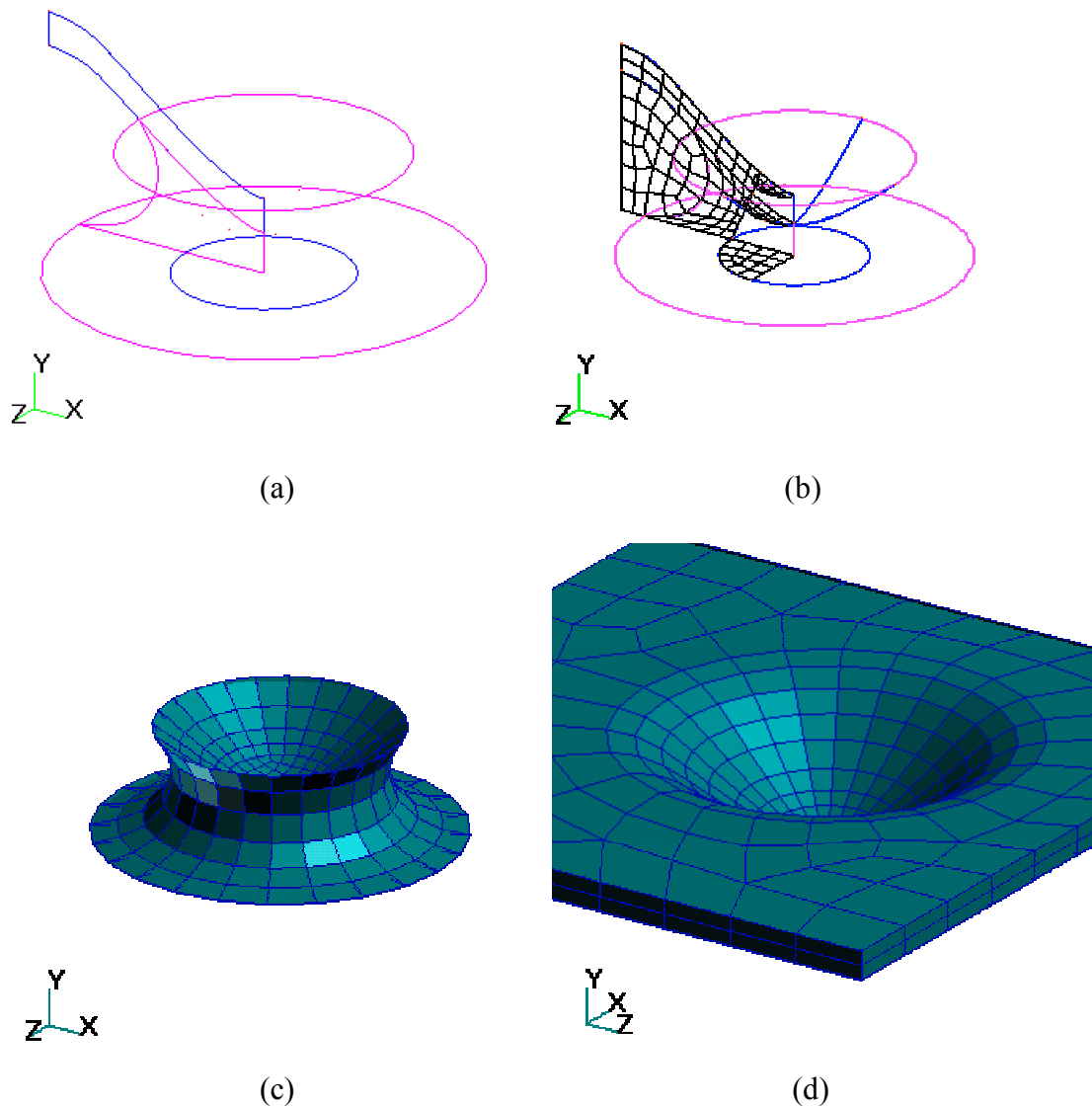


**Figure 4.13 Sample modeling process using the dimple solder joint and copper interconnect: (a) base geometry; (b) surface mesh; (c) solder joint mesh obtained from sweep of the surface mesh; and (d) copper interconnect mesh.**

#### *4.5.2.2 Modeling for the thermal cycling test*

The thermal cycling test samples are made using metallized silicon substrates and solder-attached copper flex sheets. The only boundary condition that is needed is to prevent the model from rigid body motion, which will not affect the stress and strain results. The FEM models are shown in Figure 4.14. Both the CCB and the DAI sample consist of six solder joints forming a 2 x 3 array. The footprint of the solder pad is  $1.828 \text{ mm}^2$  (radius  $0.7628 \text{ mm}$ ), and the spacing is  $2.473 \text{ mm}$  in the length direction and  $3.989 \text{ mm}$  in the width direction. The silicon pieces are dimensioned  $7.2 \times 8.9 \text{ mm}^2$ . The volume of the CCB solder joint is  $0.770 \text{ mm}^3$ , and the DAI is  $0.246 \text{ mm}^3$ . The distance between the copper interconnect (flat portion) and the silicon chip for the CCB is  $0.45 \text{ mm}$ , and is  $0.635 \text{ mm}$  for the DAI.

A uniform temperature loading of  $-55 \sim 125^\circ\text{C}$  per cycle is used, since this is the chamber temperature profile. The temperature load, simulating the solder reflow process, has been considered using linear cooling from the solder liquidus point to room temperature within 60 seconds, which means the stress-free state is selected to be at the reflow temperature.

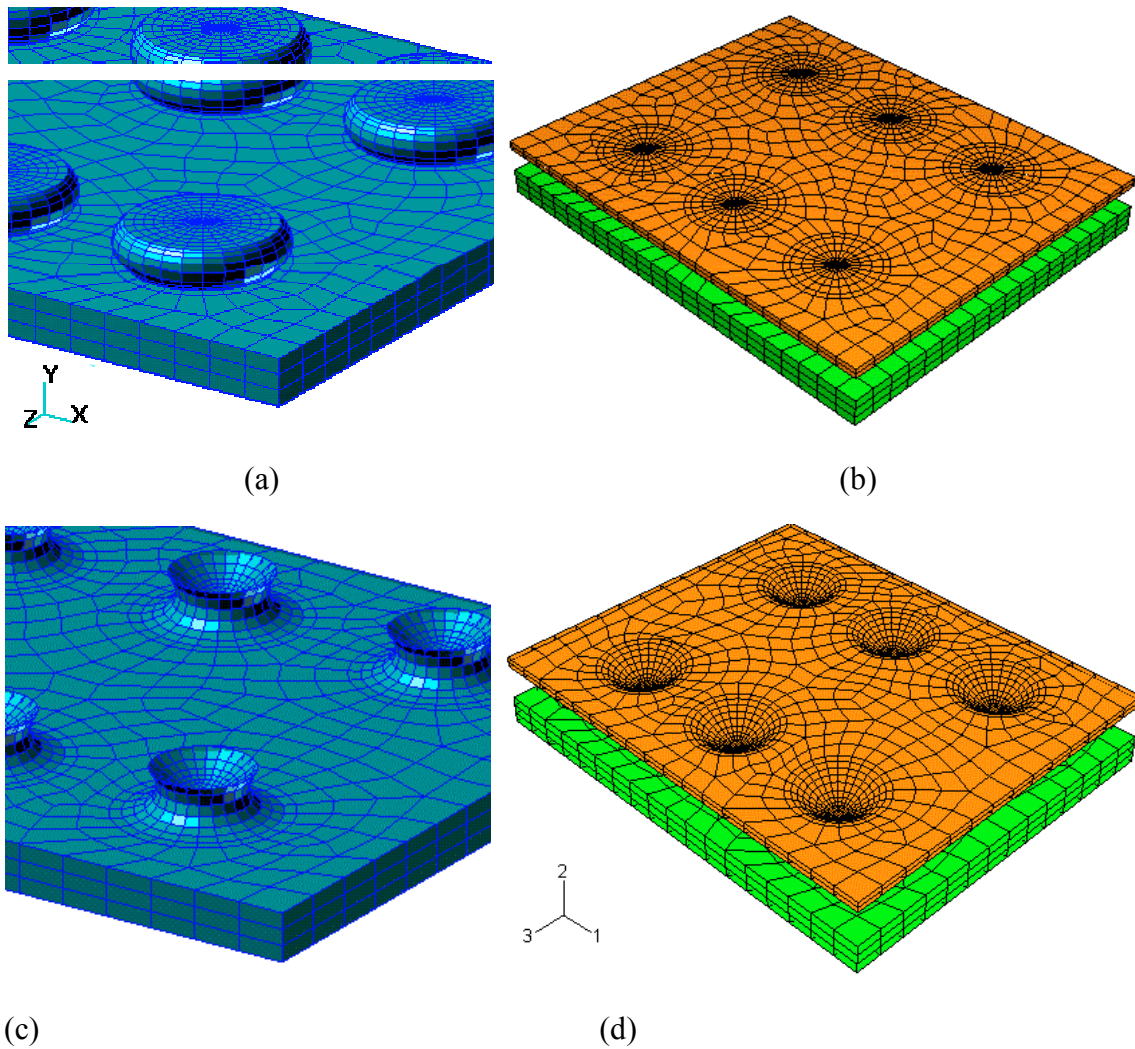


**Figure 4.14 FEM models: (a) CCB package not showing Cu; (b) full CCB package; (c) DAI package not showing Cu; and (d) full DAI package.**

#### ***4.5.2.3 Modeling for the power cycling test***

The power cycling test package consists of a bare power diode chip soldered to an alumina DBC substrate, five solder interconnects either in the Dimple Array shape or in the barrel shape (CCB), and a copper sheet. Figure 4.15 shows these two types of test packages.

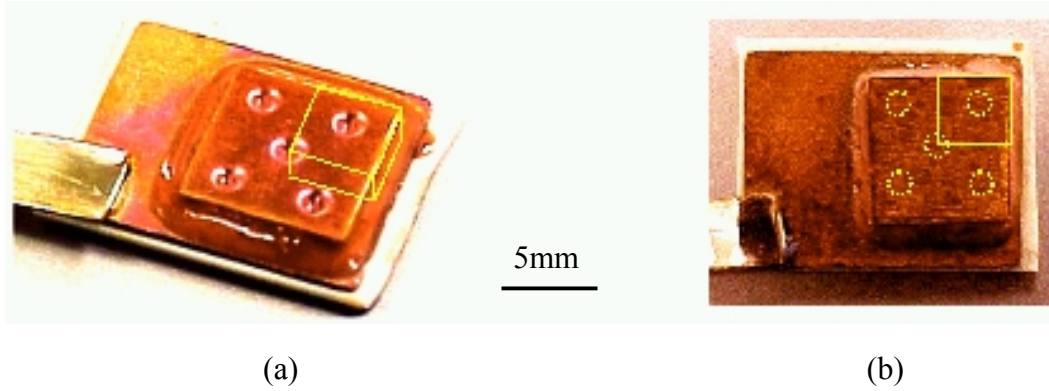


**Figure 4.15 Power cycling test sample: (a) Dimple Array package and (b) CCB package.**

The problem has been formulated by modeling a quarter of each of the two types of packages, the Dimple Array test package and the CCB package. The finite element mesh of these two models is shown in Figure 4.16. Since the research focuses on the solder joint failure, a simplification has been made to save computation time by removing the DBC substrate and the die-attach solder, replacing them with a vertical constraint on all bottom nodes of the silicon. This simplification results in more conservative results (see the discussion in Section 4.7.1).

Plane symmetry is realized using the \*EQUATION command in ABAQUS to define a linear constraint equation for the nodes on a symmetry plane. The following general expression of this linear constraint is:

$$A_1 u_i^P + A_2 u_j^Q + A_3 u_k^R = 0 \quad (\text{Eq. 4.28})$$

where  $u_i^P$  is a nodal variable at node P and at degree of freedom i, and  $A_n$  are the coefficients that define the relative motion of the nodes [160]. Therefore, the linear constraint for nodes on the 1-2 plane (Figure 4.16) is defined as:

$$u_3^P - u_3^m = 0 \quad (\text{Eq. 4.29})$$

where  $u_3^m$  is the displacement along axis 3 at a reference node m on the same plane, and  $u_3^P$  represents the displacement of each node along the 1-2 plane. Similarly, for the nodes on the 2-3 plane (Figure 4.16), the following relationship holds:

$$u_1^P - u_1^n = 0 \quad (\text{Eq. 4.30})$$

where  $u_1^n$  is the displacement along axis 1 at a reference node n on the same plane. If one-eighth is modeled instead of a quarter, this linear constraint on the 45° planes, say between +x and +z direction, becomes:

$$u_1^P - u_3^n = 0 \quad (\text{Eq. 4.31})$$

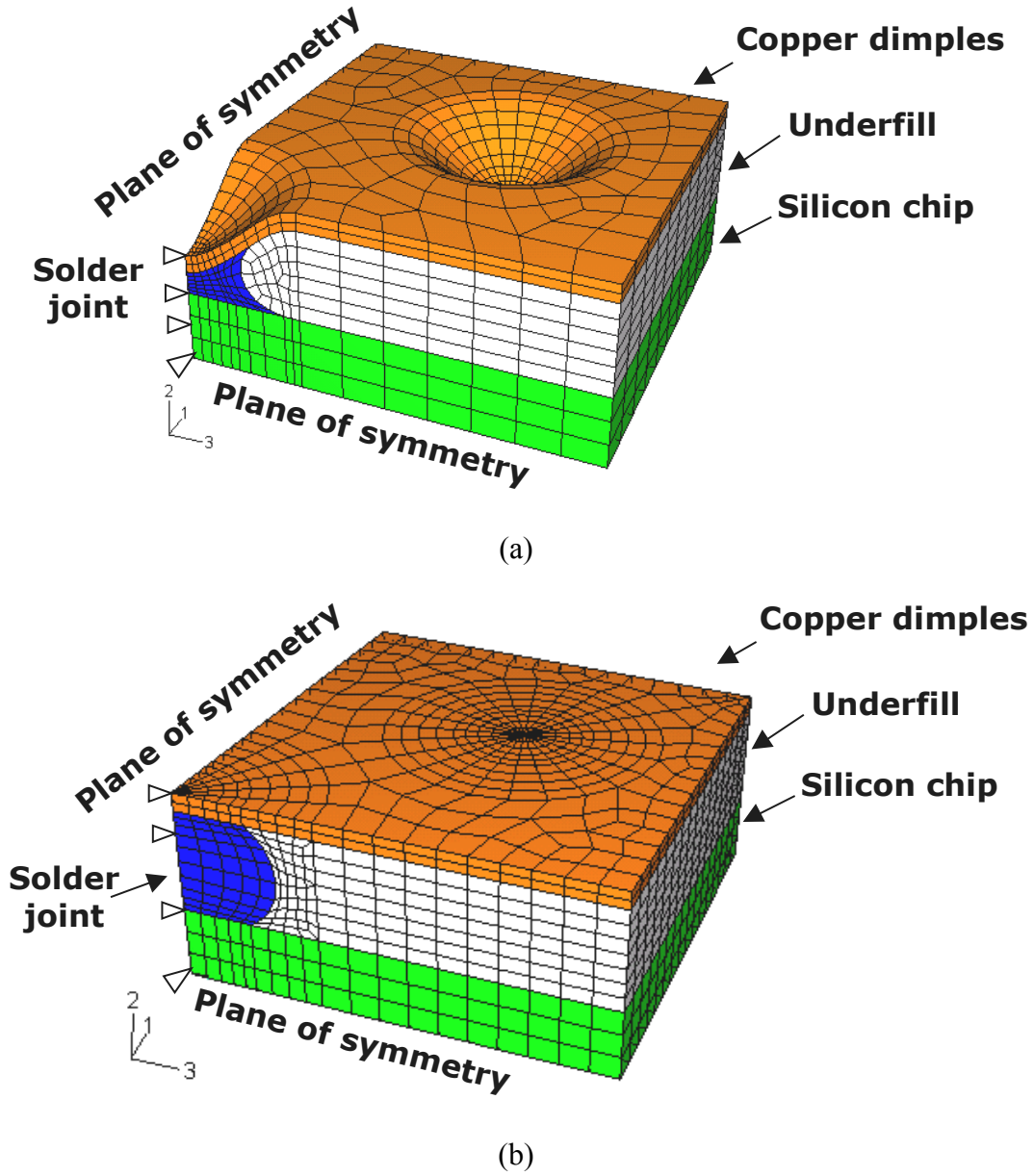


Figure 4.16 FEM models for (a) the DAI and (b) the CCB.

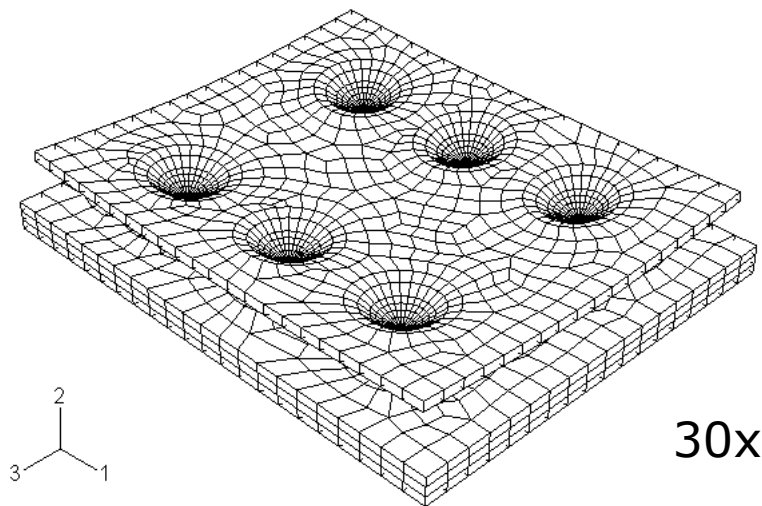
A uniform temperature load of 10~100°C per cycle is used based on the measured temperature at the copper interconnect. The temperature load simulating the solder reflow process has been considered using a linear cooling from 183°C to room temperature for eutectic Pb37-Sn63 solder.

## 4.6 FEM modeling results

### 4.6.1 Thermal cycling

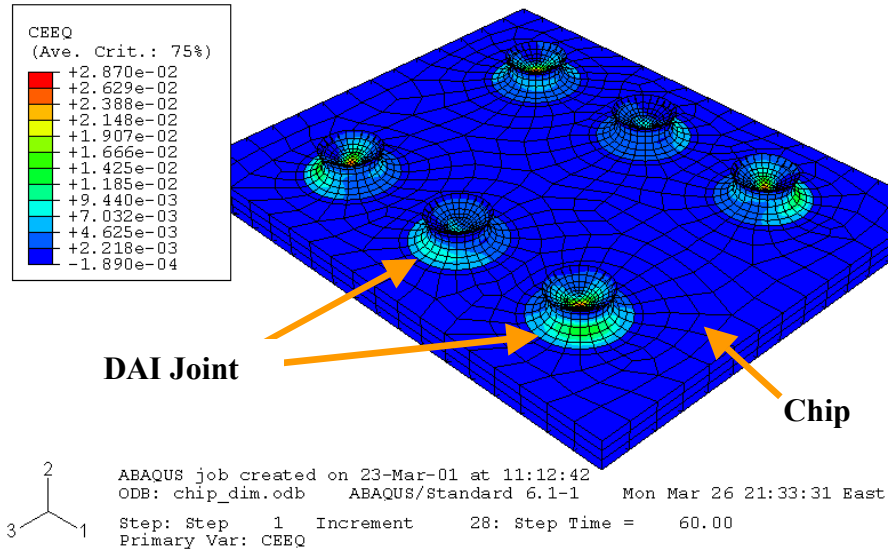
All FEM models in this section are for non-underfilled packages.

Figure 4.17 shows the deformation of the DAI sample (magnification is 30x) at -55°C. Due to the constraint from the dimple solder joints, the dimple interconnect warped.



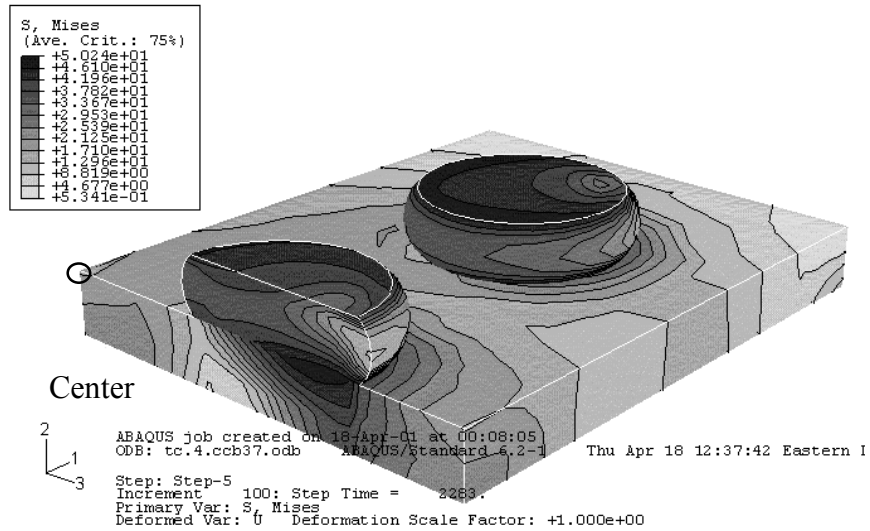
**Figure 4.17 Deformation of the Dimple Array package at the cold extreme (-55°C), 30x magnification.**

Figure 4.18 shows the CEEQ contour of the DAI (the copper interconnect is hidden for clarity) after the initial cooling from reflow temperature. The PEEQ contour is similar to this. Because of the shape of the dimple, the solder joints experience different degrees of inelastic strains. However, they have one thing in common: Every solder joint has more deformation on the far side from the neutral point, which is the center of the chip.

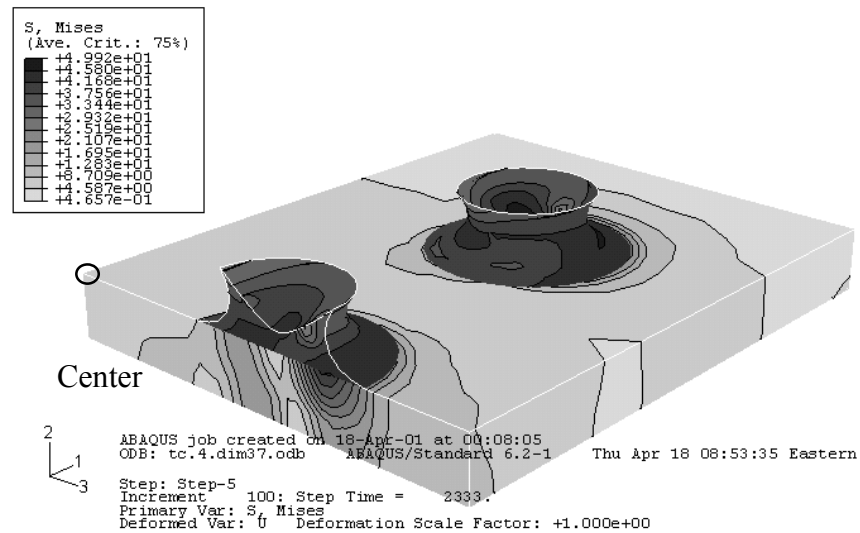


**Figure 4.18 CEEQ contour of the DAI after the initial cooling stage.**

A comparison of the Mises stress distribution for the CCB sample and the dimple sample at  $-55^{\circ}\text{C}$  is shown in Figure 4.19 (copper flex is not shown for clarity). The FEM models shown here are a quarter of the overall models, with the chip center located at the left corner of the chip. Because the temperature cycling samples were not underfilled, the CTE mismatch between the copper and the silicon has been mostly loaded to the solder joints, even though the deformation of the copper interconnect flex helps reduce the stresses exerted on the solder joints. The major driving force for these inelastic deformations is the von Mises stress, which is responsible for changing the shape and distortion of the material. Evidence for this can be found by the noticeable similarity between the von Mises stress contour and the inelastic strain contour (CEEQ or PEEQ), as shown in Figures 4.20 and 4.21. It is also found that the Mises stresses are highest when the temperature is at the cold extreme, which is  $-55^{\circ}\text{C}$ . This suggests that more damage occurs at the cold stage of the temperature cycling experiment.



(a)



(b)

**Figure 4.19 Von Mises stress distribution in (a) CCB models and (b) DAI models (Chip center is marked with circle on the left side).**

Figures 4.20 and 4.21 show the CEEQ and PEEQ of the CCB solder joint and the dimple solder joint at the end of the third thermal cycles. Since the CEEQ and PEEQ are positive values that describe the accumulated fatigue damage imposed on the solder joints, the values shown in the figures include the initial CEEQ and PEEQ caused by cooling from the reflow temperature to room temperature. It is shown in these contours that the CEEQ is significantly larger than PEEQ (remark: eutectic Pb-Sn solder is stiffer at low

temperature than most of other solders), and that both the CEEQ and the PEEQ in the CCB solder joint are larger than those of the dimple solder joint. Another important difference is that in the CCB solder joint, the strain concentration is highly localized at the edge of the solder/chip interface, while in the dimple solder joint, the strain concentration is distributed more uniformly throughout the whole solder joint. The smaller solder volume needed for the same solder pad area and the dimple solder fillet that eliminates the structural singularity largely lead to this difference.

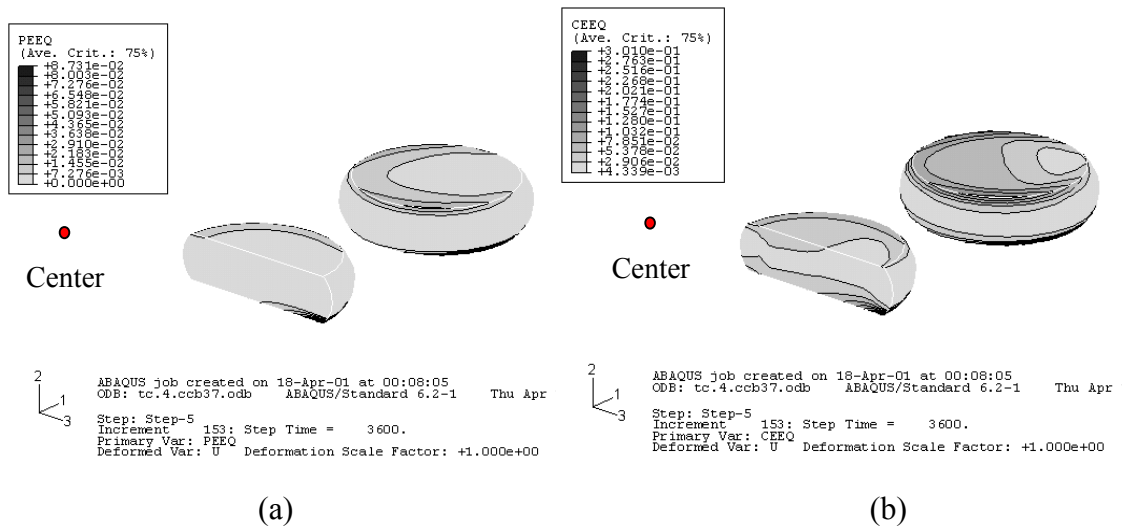


**Figure 4.20 CCB solder joints strain contours: (a) PEEQ and (b) CEEQ (the chip center is to the left).**

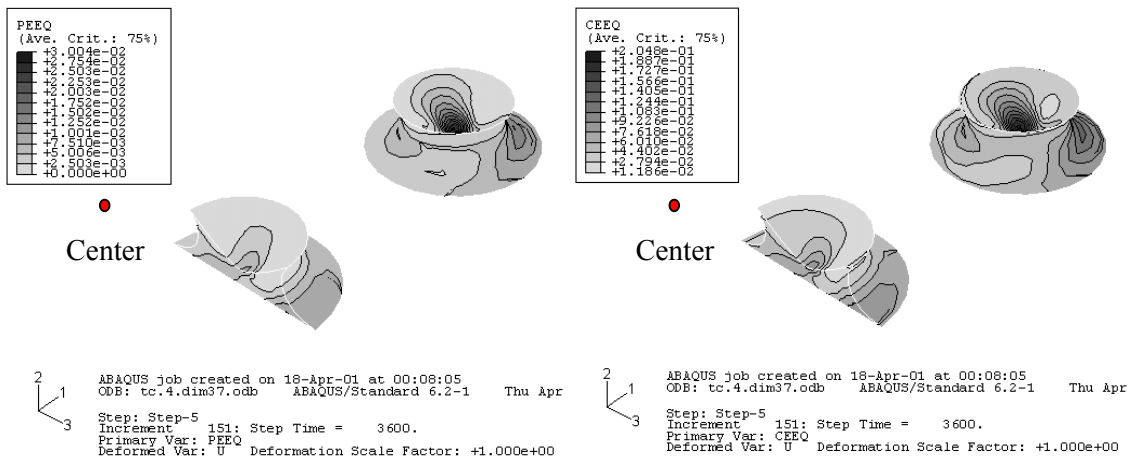


**Figure 4.21 DAI solder joints strain contours: (a) PEEQ and (b) CEEQ (the chip center is to the left).**

It is noted that the silicon side-solder of the CCB solder joint experiences more deformation than the copper side. The weakest location on the CCB is the outer edge of the solder close to the chip, while the weakest location for the dimple is the center near the solder/copper interface.

In order to better understand the complex stress/strain state that occurs in the solder joints during temperature cycling, von Mises stress components at the weakest locations are plotted in Figure 4.22. As previously discussed, the Mises stress components are taken from the cold temperature extreme (in the third cycle) because the Mises stress reaches the highest value at this point. In this figure,  $S_{ij}$  represents the stress tensor.

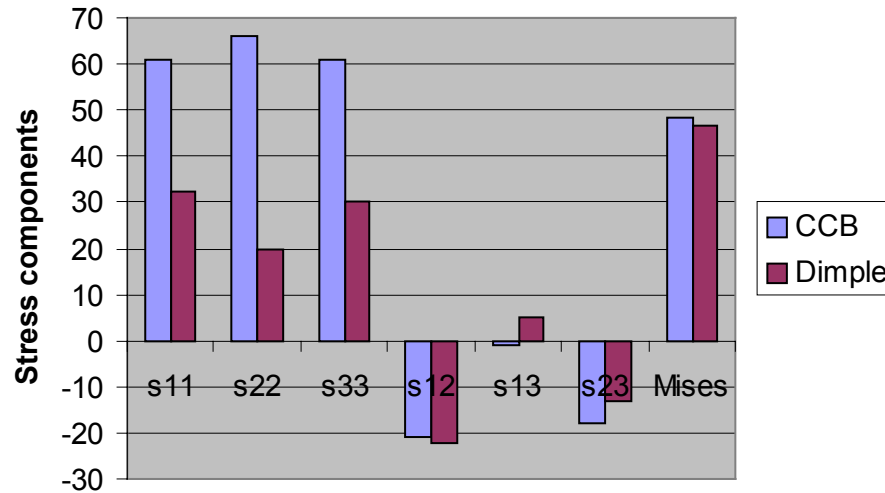


**Figure 4.22** Stress components at the weakest locations in solder joints; cold extreme.

As shown in Figure 4.22, both the CCB and the dimple have fairly high normal stresses ( $s_{11}$ ,  $s_{22}$  and  $s_{33}$ ) at their weakest locations. However, these normal stresses do not necessarily lead to large normal strains due to the effects of hydrostatic pressure. The von Mises yield criterion states that

$$\sigma_0 = \sqrt{\frac{1}{2}[(\sigma_{xx} - \sigma_{yy})^2 + (\sigma_{yy} - \sigma_{zz})^2 + (\sigma_{zz} - \sigma_{xx})^2 + 6\tau_{xy}^2 + 6\tau_{yz}^2 + 6\tau_{zx}^2]} \quad (\text{Eq. 4.32})$$

Since the yield criterion is based on differences in normal stresses,  $\sigma_{xx} - \sigma_{yy}$ , etc., in the case when all three normal stress components are close in value, it is the shear stresses that contribute the majority of the yield of the solder joint. Theoretically, the von Mises criterion is a maximum-distortion-energy criterion because it was shown by Hencky (1924) that this equation is equivalent to assuming that yielding occurs when the distortion energy reaches a critical value [153].

The comparison of strain components further proves this. In Figure 4.23 the maximum shear strain components  $e_{12}$  ( $\epsilon_{12}$ ) and  $e_{13}$  ( $\epsilon_{13}$ ) are major contributors to CEEQ and PEEQ. Much higher shear strains are found in the weakest locations of the CCB solder joints than occur in the dimple solder joint.

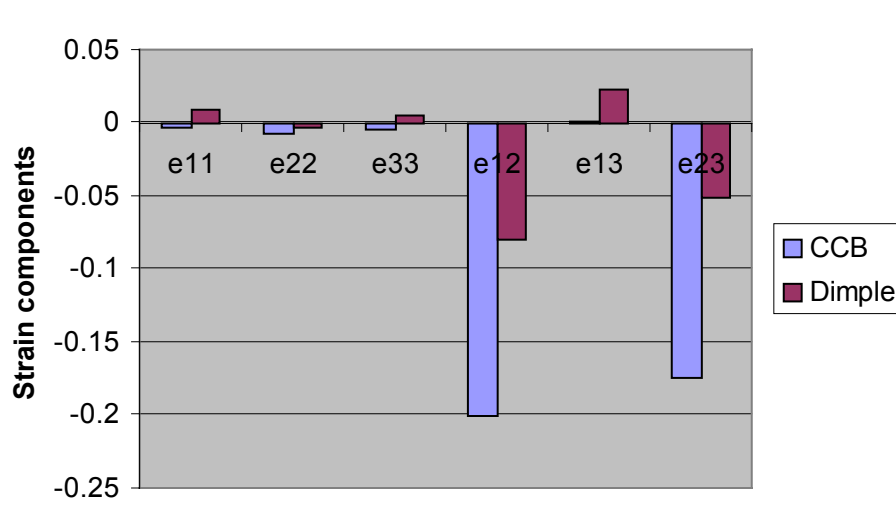


**Figure 4.23 Strain components at weakest locations in solder joints; cold extreme.**

The histories of CEEQ and PEEQ for the weakest locations of both CCB and dimple solder joint are shown in Figure 4.24. This graph shows that creep damage is the dominating factor for temperature cycling of the eutectic tin-lead solder joint in either the CCB or the dimple shape. The CEEQ range (increment per temperature cycle) of the CCB solder joint is much larger than that of the dimple solder joint. The rate of PEEQ and CEEQ accumulation reaches a saturated state after just three cycles.

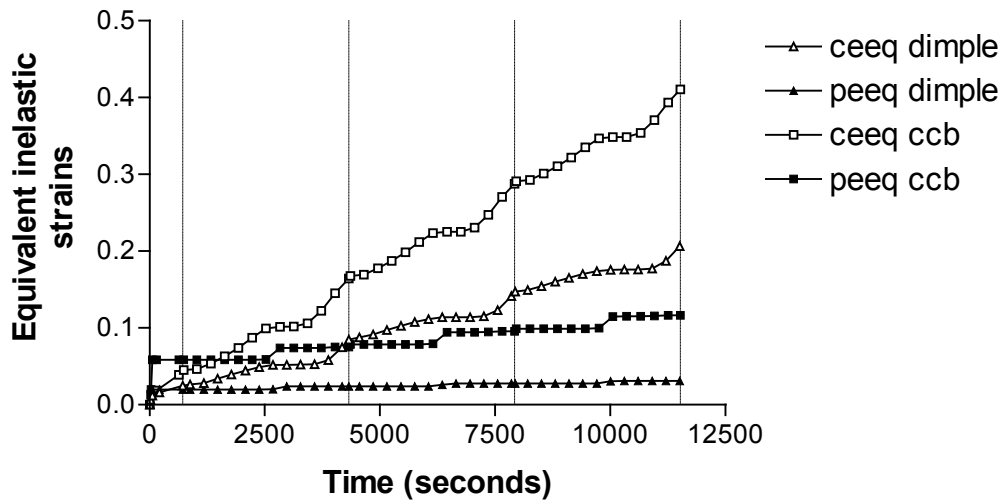


**Figure 4.24 Equivalent inelastic strain (CEEQ and PEEQ) histories in solder joints.**

The stress-strain hysteresis loops (solder ratcheting), in this case  $\tau_{12}$ - $\gamma_{12}$  hysteresis loops, are shown in Figure 4.25 for both CCB and dimple solder joints. This type of curve represents the cyclic strain response that occurred during temperature cycling. In this figure, shear stresses are negative at cold extremes and positive at hot extremes. Shear strains are ratcheting toward the negative side of the strain axis with time, because due to inelastic strain damage (creep and plasticity), the stress/strain cannot fully recover to the starting state of last cycle. It is clearly seen that at the cold extreme of the temperature cycling ( $-55^{\circ}\text{C}$ ), the shear stress is much higher than at the hot extreme ( $125^{\circ}\text{C}$ ), indicating that the interfacial adhesion problem might most likely occur at low temperatures. It is obvious that the ratcheting curves of the dimple solder joint are much more stable than those of the CCB solder joint. The smaller shear strain range of the DAI also suggests that temperature cycling incur less damage per cycle in the DAI than in the CCB.

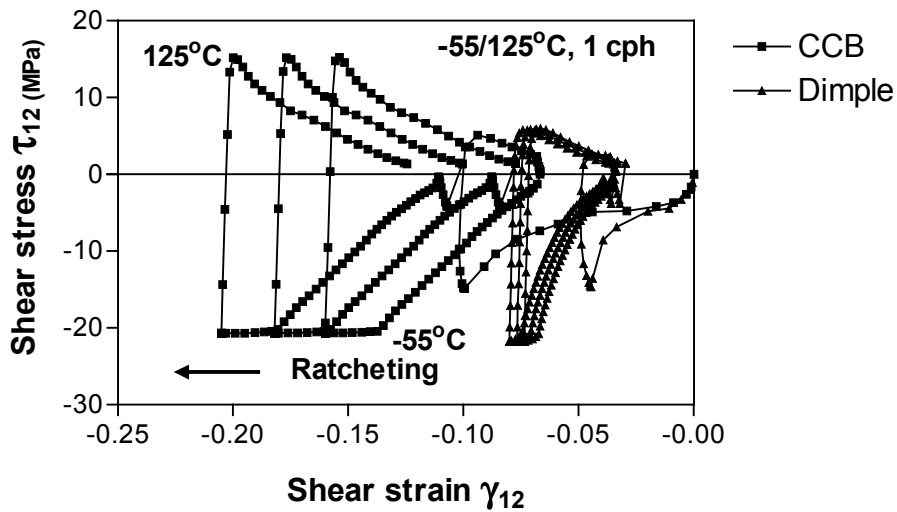


Figure 4.25 Shear stress-strain hysteresis loops of the CCB and dimple solder joints.

#### 4.6.2 Power cycling

##### 4.6.2.1 Modeling results for Pb37-Sn63, non-underfilled cases

Figure 4.26 shows the von Mises stress contour of the DAI package at the cold extreme (10°C) of the fourth power cycles. The left corner is the chip center. Stresses are fairly uniformly distributed within solder joints. Compared with the temperature cycling case, the von Mises stresses are much lower under power cycling. The weakest location is at the solder/silicon interface.

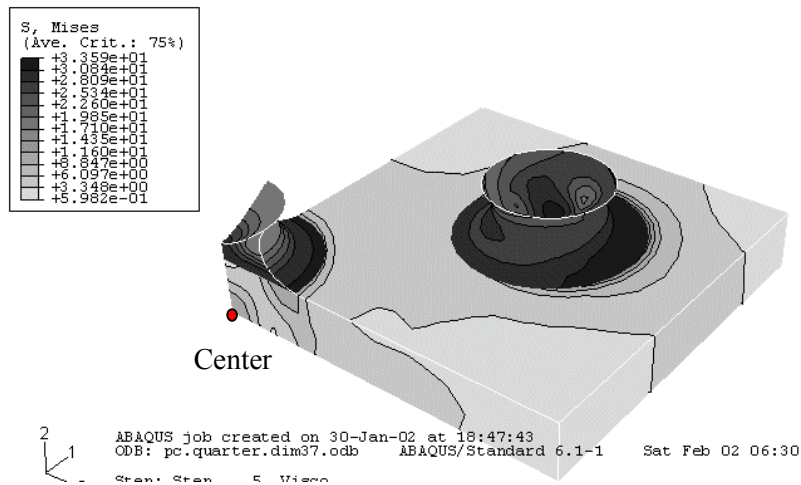
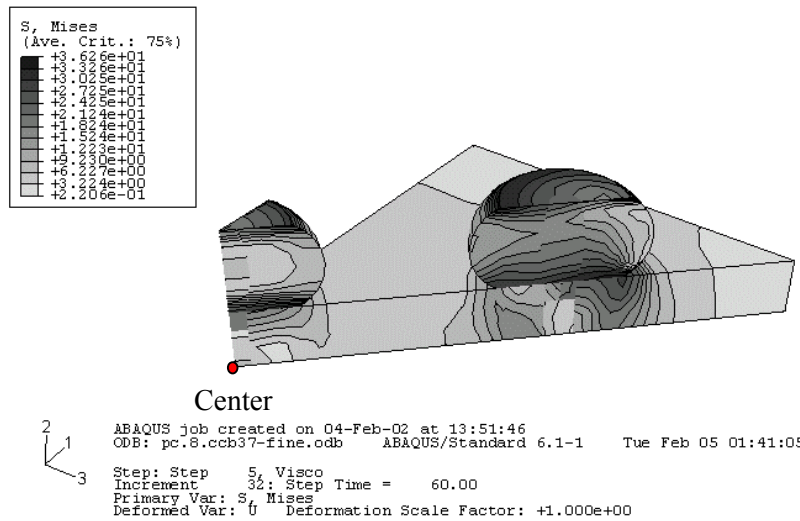


Figure 4.26 Von Mises stress contours in the dimple solder joints at the cold extreme.

Figure 4.27 shows the von Mises stress for the CCB solder joint (one-eighth model). The left corner is the chip center. Stresses are localized at the corners of the solder joint at the Si/solder and solder/copper interfaces. Comparison of the von Mises stress distribution between the CCB and the dimple indicates that the average stress level is higher in the dimple solder joint.



**Figure 4.27 Von Mises stress contours in the CCB solder joints at the cold extreme.**

Figure 4.28 shows the equivalent inelastic strain histories (CEEQ and PEEQ) for both CCB and dimple solder joints (non-underfilled) at their weakest locations. Except for the first 60 seconds of cooling from the reflow temperature, the dotted lines divide the simulation time into four power cycles. A major difference between this plot and the temperature cycling plot is that creep deformation does not dominate the fatigue damage in the CCB solder joint. In the dimple solder joint, however, the PEEQ is much lower than the CEEQ. The initial damage due to reflow cooling is large compared to the inelastic strain per cycle. Again, the rate of PEEQ and CEEQ accumulation reduces and reaches a saturated state after just three cycles.

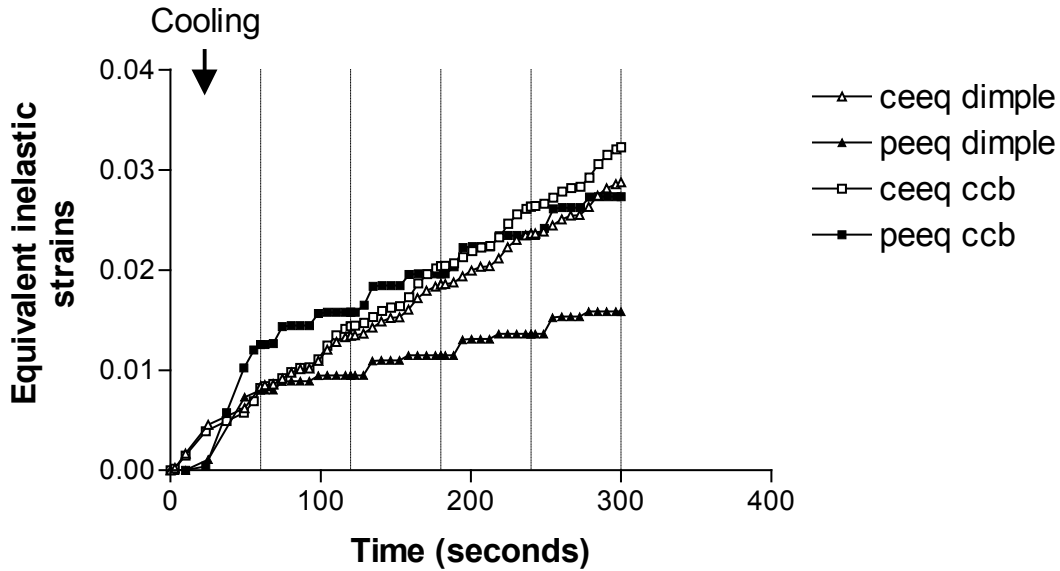


Figure 4.28 Equivalent inelastic strain histories for power cycling.

#### 4.6.2.2 Modeling results for Pb37-Sn63, underfilled cases

Figure 4.29 shows the contour of accumulative equivalent plastic strain. After four cycles, the dimple joint (underfilled sample) has the highest accumulative equivalent plastic strain,  $5.07 \times 10^{-3}$ , at the center of the joint (location A, close to the copper/solder interface). This is different from the non-underfilled case, for which the highest PEEQ occurs at the silicon/solder interface (site B). Still, the CCB joint is weakest at the outer corner of the solder joint (silicon/solder interface), with a total equivalent plastic strain of  $5.24 \times 10^{-3}$  for the first four cycles.

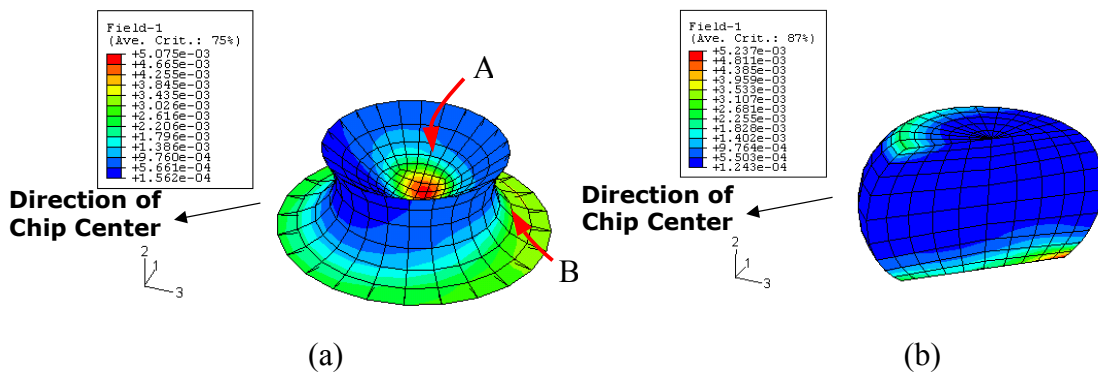


Figure 4.29 Total accumulative equivalent plastic strain for first four cycles: (a) DAI and (b) CCB solder joint.

The equivalent plastic strain range (accumulation per cycle), however, differs dramatically between these two types of solder joints. The dimple joint experiences a higher initial equivalent plastic strain and then stabilizes to a smaller increment value per cycle than the CCB joint. The same behavior applies to equivalent creep strains. A comparison of these two terms is shown in Table 4.4. The total equivalent inelastic strain per cycle listed in the table is simply the sum of the creep and the plastic strains per cycle. It is compared to illustrate that the equivalent plastic strain (PEEQ) in the weakest location of the CCB solder joint is much larger than that in the dimple solder joint.

**Table 4.4 Comparison of the equivalent creep, plastic and total inelastic strain per cycle.**

<i>Saturated strain range</i>	<i>Dimple, location A</i>	<i>Dimple, location B</i>	<i>CCB</i>
Equiv. Creep (CEEQ)	0.0041	0.00398	0.00528
Equiv. Plastic (PEEQ)	0.00062	0.0009	0.0035
Total Inelastic strain range	0.00472	0.00488	0.00878

## 4.7 Discussions

### 4.7.1 DBC and die-attach effects

Power cycling models with and without DBC were examined. The strain ranges and the highest stresses are compared in Table 4.5. It is seen that there is about a 20% difference between the IEEQ values. The “no-DBC” case is more conservative and predicts a higher inelastic strain range.

**Table 4.5 Strain ranges and the maximum stress at the cold extreme for the no-DBC case and the with-DBC case.**

	<i>No DBC</i>	<i>With DBC</i>	<i>Difference</i>
CEEQ	0.061	0.052	17.31%
PEEQ	0.0036	0.00227	58.59%
IEEQ	0.0646	0.05427	19.03%
Mises (MPa) at 10°C	48	48	0.00%

## 4.7.2 Correlation between FEM and experiments

### 4.7.2.1 Thermal cycling correlation

Although there are many empirical relationships involved in obtaining a prediction of solder joint fatigue life, a modified Coffin-Manson equation based on the conventional creep and plastic theory and a constitutive theory of isotropic thermoviscoplasticity [161] is used in this study to estimate the fatigue life of dimple and CCB solder joints in power device applications. The conventional creep and plastic theory assumes that there is no interaction between creep and plasticity. The total strain rate tensor is given by:

$$\dot{\boldsymbol{\varepsilon}}_{ij} = \dot{\boldsymbol{\varepsilon}}_{ij}^{el} + \dot{\boldsymbol{\varepsilon}}_{ij}^{cr} + \dot{\boldsymbol{\varepsilon}}_{ij}^{pl} + \dot{\boldsymbol{\varepsilon}}_{ij}^{th} \quad (\text{Eq. 4.33})$$

where the total strain rate tensor  $\dot{\boldsymbol{\varepsilon}}_{ij}$  is the sum of the elastic, creep, plastic and thermal strain rate tensor. And as a reminder: the equivalent plastic strain  $\boldsymbol{\varepsilon}_{eq}^{pl}$  (PEEQ) and the

equivalent creep strain  $\boldsymbol{\varepsilon}_{eq}^{cr}$  (CEEQ) are defined as:  $\boldsymbol{\varepsilon}_{eq}^{pl} = \int_0^t d\boldsymbol{\varepsilon}_{eq}^{pl} dt$  and  $\boldsymbol{\varepsilon}_{eq}^{cr} = \int_0^t d\boldsymbol{\varepsilon}_{eq}^{cr} dt$ ,

respectively, where  $d\boldsymbol{\varepsilon}_{eq}^{pl} = \sqrt{\frac{2}{3}} d\boldsymbol{\varepsilon}_{ij}^{pl} d\boldsymbol{\varepsilon}_{ij}^{pl}$  and  $d\boldsymbol{\varepsilon}_{eq}^{cr} = \sqrt{\frac{2}{3}} d\boldsymbol{\varepsilon}_{ij}^{cr} d\boldsymbol{\varepsilon}_{ij}^{cr}$  [162] (for explanation of  $d\boldsymbol{\varepsilon}_{ij}^{pl}$  and  $d\boldsymbol{\varepsilon}_{ij}^{cr}$  refer to Section 4.5.1).

The modified Coffin-Manson equation relates the equivalent inelastic strain per cycle  $\Delta\boldsymbol{\varepsilon}_{eq}^{in}$  (sum of CEEQ and PEEQ) to lifetime (actually, the crack initiation time) of eutectic tin-lead solder joints using Eq. 4.34:

$$N_{50} = B_1 (\Delta\boldsymbol{\varepsilon}_{eq}^{in})^C \quad (\text{Eq. 4.34})$$

where

$N_{50}$  is the mean fatigue life,

$\Delta\boldsymbol{\varepsilon}_{eq}^{in}$  is the accumulated equivalent inelastic strain per cycle,

$B_1$  is the material constant, 0.146 for eutectic solder [163], and

$C$  is the material constant, -1.94 for eutectic solder [163].

It must be pointed out that the material constants B1 and C are highly sensitive to the package type, solder pad size and solder volume, and the dominant fatigue mechanism (creep versus plasticity) [151]. Therefore, it is not realistic to expect a perfect match between experiment and life prediction using this set of material constants, especially when the package materials used in the CBGA and the DAI are totally different (copper instead of ceramic substrate in C4/BGA application).

Table 4.6 shows the predictions and the experimentally obtained results for the thermal cycling test.

**Table 4.6 FEM predictions and experimental results for thermal cycling.**

<i>Saturated strain range</i>	<i>Dimple, location A</i>	<i>Dimple, location B</i>	<i>CCB</i>
Equiv. Creep $\Delta\epsilon_{eq}^{cr}$ (CEEQ)	0.0617	0.0424	0.1230
Equiv. Plastic $\Delta\epsilon_{eq}^{pl}$ (PEEQ)	0.0036	0.0020	0.0207
Equiv. Inelastic $\Delta\epsilon_{eq}^{in}$	0.0653	0.0444	0.1437
Predicted $N_{50}$ (cycles)	29	61	6.3
Experimental results (20% increase of dc resistance)	110		8
Experimental results (50% increase of dc resistance)	185		23

The reliability improvement of the Dimple Array in the temperature cycling test is  $110/8 = 14x$  (20% resistance increase) and  $185/23 = 8x$  (50% resistance increase). The FEM modeling result is  $29/6.3 = 4.6x$  at location A and  $61/6.3 = 9.7x$  at location B.

Since in the thermal cycling test most of the failures are UBM delamination, a comparison of the normal stress at the device surface is worthwhile. Figure 4.30 compares the normal stress S22 (denotes  $\sigma_{22}$ ) in the CCB (a) and Dimple Array (b) models at the solder/device interface. It is clearly shown that significantly larger normal stress in the CCB solder joint leads to early UBM delamination failure.

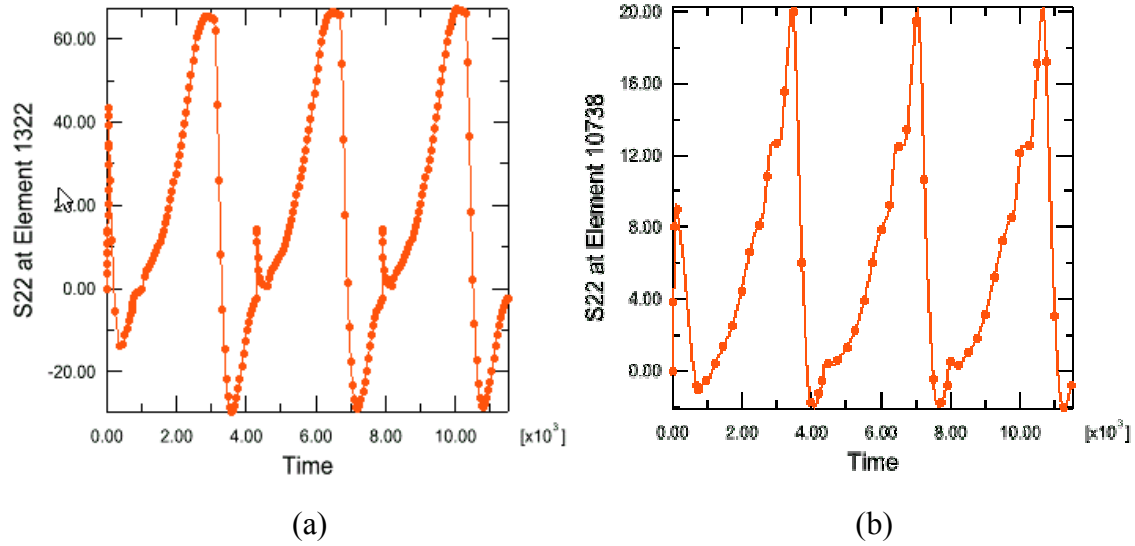


**Figure 4.30** Normal stresses S22 at the solder/device interface for (a) CCB and (b) DAI.

#### 4.7.2.2 Power cycling correlation

Due to the fact that the power cycling test could not offer a credible estimate of time-to-crack-initiation, it is impossible to correlate the FEM modeling fatigue life prediction with experiments. For the completeness of this work, the FEM-predicted mean time-to-crack-initiation is shown in Table 4.7. It needs to be mentioned that the modeling did not include DBC and die-attach material. Since from previous discussion, the saturated inelastic strain range  $\Delta\epsilon_{eq}^{in}$  calculated using simplified models is 20% larger than the models incorporating DBC and die-attach solder, a modification is necessary to obtain more accurate results.

**Table 4.7** Prediction of crack initiation time using FEM.

<i>Inelastic strain range</i>	<i>Dimple, A</i>	<i>Dimple, B</i>	<i>CCB</i>
Without DBC $\Delta\epsilon_{eq}^{in}$	0.00472	0.00488	0.00878
Modified $\Delta\epsilon_{eq}^{in}$	0.00393	0.00407	0.00732
Predicted $N_{50}$ (cycles)	6780	6335	2029

Nevertheless, it is possible to correlate the failure mechanisms predicted by FEM with those obtained from the failure analysis of experimental samples. Figure 4.31 shows a typical cross-section of a failed Dimple Array solder joint. This is an optical microscopy image taken from a Dimple Array solder joint after 12,700 power cycles from 10°C to 100°C. The FEM-predicted maximum inelastic strain distribution is shown on the right (viewport angle in PATRAN/insight: (15.83 54.4 1.41)). It is clearly shown that the cracks roughly correlate with the regions having the largest inelastic strains.

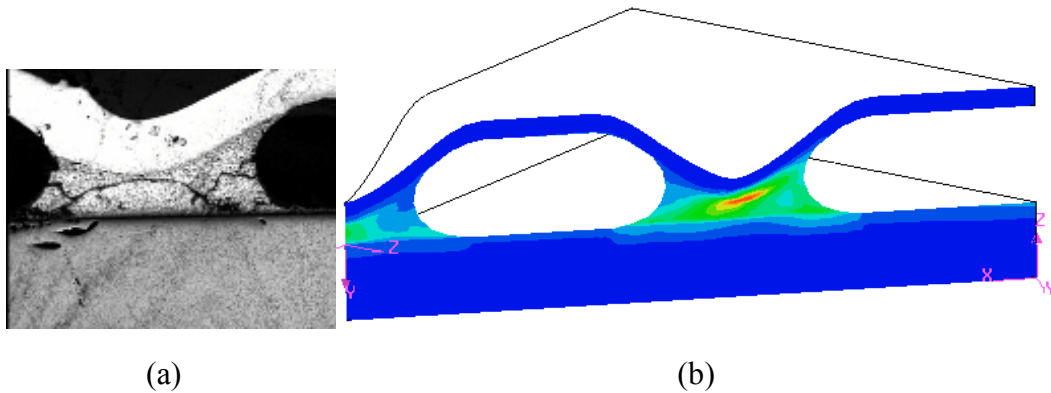


**Figure 4.31 Correlation: (a) optical microscopy image of a DAI joint (12,700 cycles); and (b) the FEM predicted inelastic strain distribution.**

Figure 4.32 shows an SEM image of a typical CCB joint after 8,500 power cycles from 10°C to 100°C, and the FEM-predicted maximum inelastic strain distribution. Since the highest strain concentration occurs at the solder/device interface, this is where the crack initiates and grows.

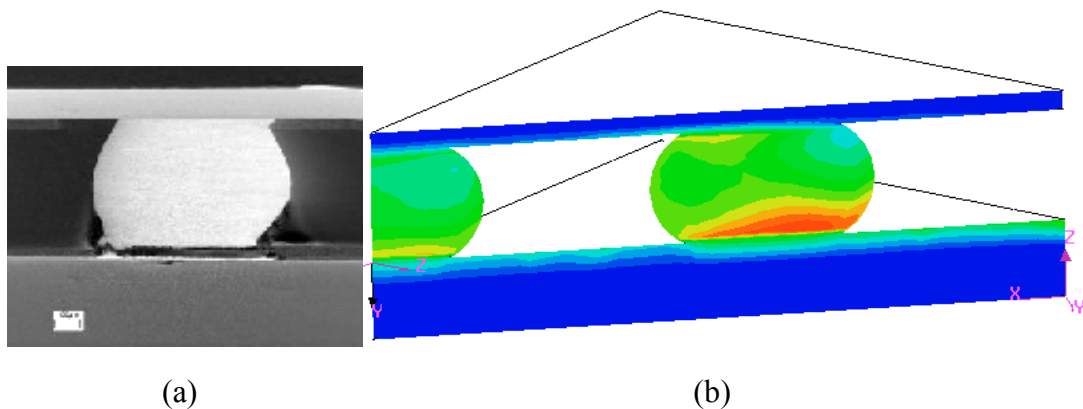


**Figure 4.32 Correlation: (a) SEM image of a CCB joint (8,500 cycles); and (b) the FEM predicted inelastic strain distribution.**

Both the dimple and the CCB failure modes are in excellent agreement with the FEM modeling results.

### 4.7.3 Discussion of various modeling issues

#### -Residual stresses

The effects of the residual stress can be directly obtained from the modeling results. Figure 4.33 shows the Mises stress history, the creep strain and the plastic strain histories, and the temperature history for reflow-cooling and the first power cycle of a selected weakest spot in the dimple solder joint (eutectic tin-lead).

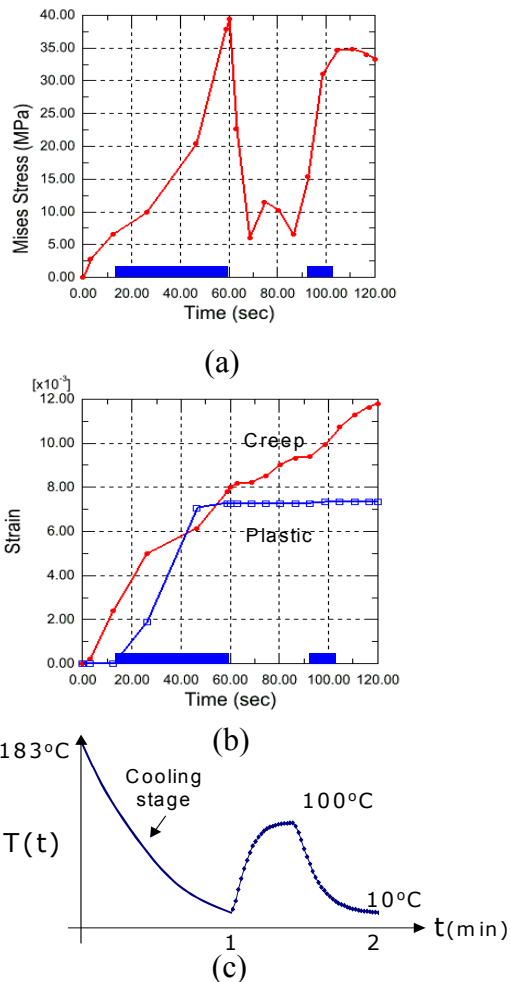


**Figure 4.33 History of the eutectic DAI solder joint:**  
**(a) Mises stress; (b) strain; and (c) temperature.**

This graph shows an initial stress-/strain-free state, followed by a dramatic increase in both, with a peak Mises stress of 40MPa for the eutectic tin-lead solder at low temperature (10°C), and a large amount of creep and plastic strain occurring during this period. In the following power cycle, the package is gradually heated up to 100°C in 25 seconds with no plastic deformation. Creep continues to develop, and the Mises stress decreases because the assembly is going back toward the original stress-free state. However, before the temperature reaches 100°C, the stress starts to increase again. This is because the irreversible plastic and creep damage during the reflow-cooling stage prevents the solder joint from a full recovery. It is interesting that just before the temperature reaches 100°C, the stress relaxes. This is due to the continuous development of creep at the high-temperature dwell time. The stress history in the following power cycles basically follows a similar pattern: the structure relaxes at high temperatures, and shows high stress levels at low temperatures.

One other important note is that for the eutectic tin-lead solder (hard solder), subsequent power cycles do not cause much plastic damage after the initial deformation, because the solder rarely experiences a stress higher than the yielding strength at each temperature level. This explains why the eutectic tin-lead solder has a stronger plastic resistance.

Another set of simulations has been performed to study the effects of the selection of an initial stress-free temperature using the non-underfilled Dimple Array model (power cycling). The following graphs (Figure 4.34) illustrate the difference in the temperature profile and von Mises stress history. If the residual stress due to solder reflow is considered, a large von Mises stress spike is present at the end of the cooling stage due to the fact that the solder becomes stronger at lower temperatures. When the first power cycle starts, the stress quickly relaxes. In the case for which no residual stress is considered (stress-free at 10°C), such a stress spike does not exist. Overall, in the consecutive power cycles, the no-residual stress simulation shows a result that very closely resembles the more accurate model that includes the residual stress consideration: high stress occurs at the cold extreme and low stress at the hot extreme; even the actual stress values are very close. The difference only appears in the first cycle.

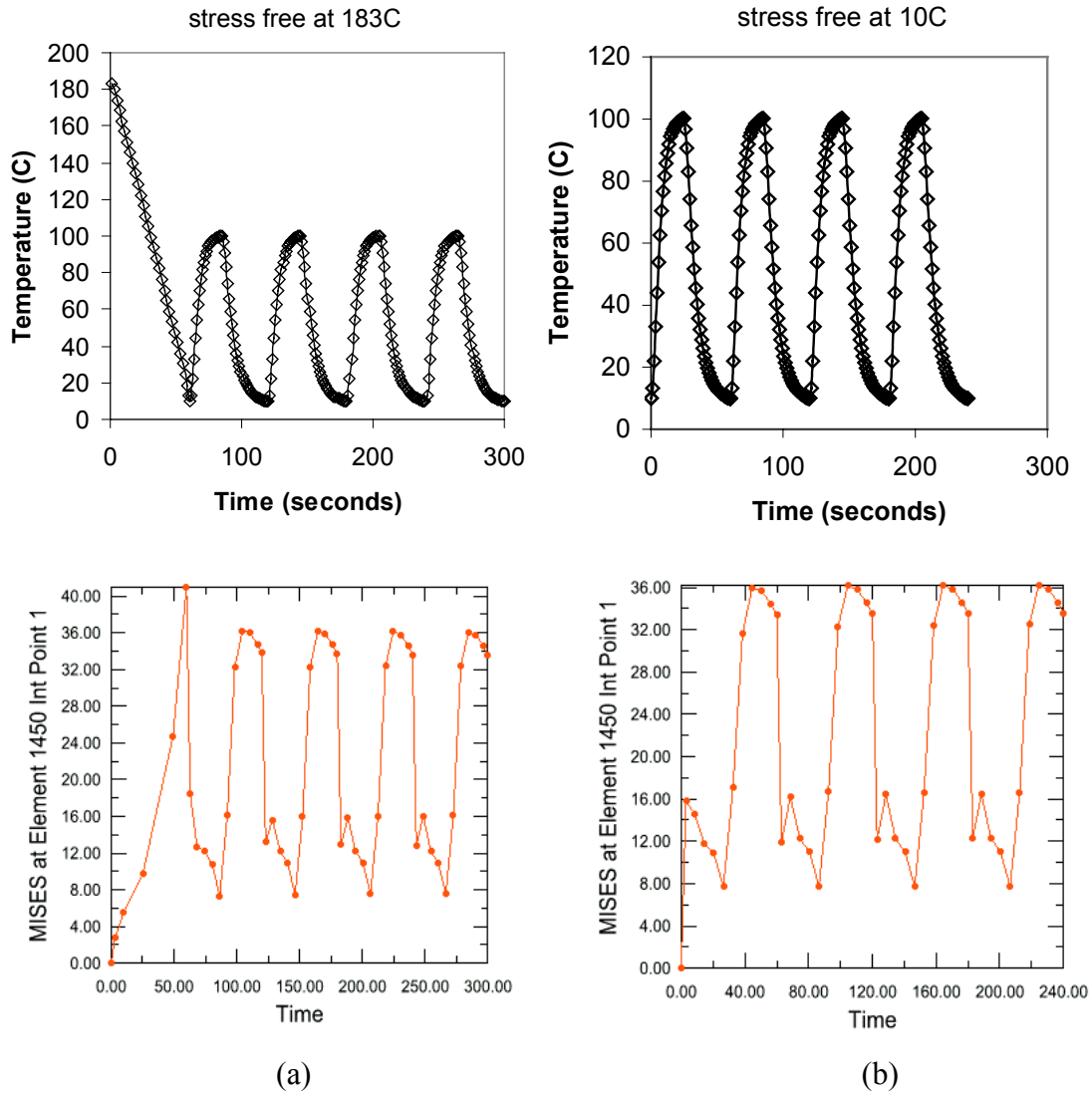


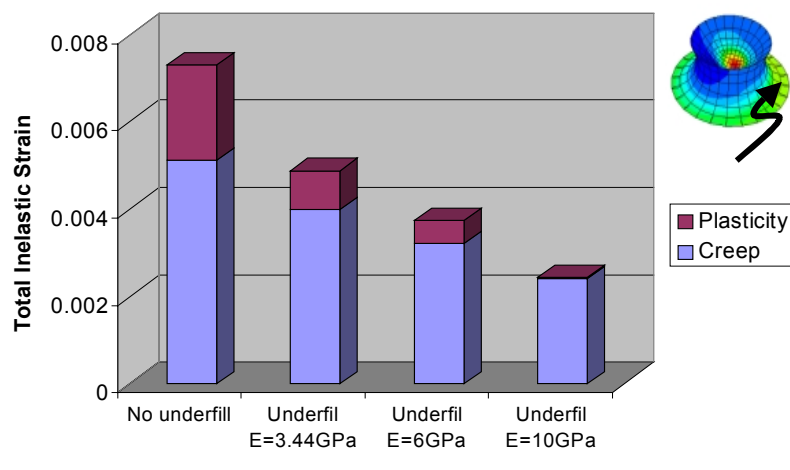
**Figure 4.34 Temperature profile (top) and von Mises stress (bottom) for a case study that considers residual stress (a) and omits residual stress (b).**

Other characteristics, such as the inelastic strain range, also suggest that residual stress does not appear to have strong effects on material behavior in subsequent cycles. This result is in close agreement with previous work [164].

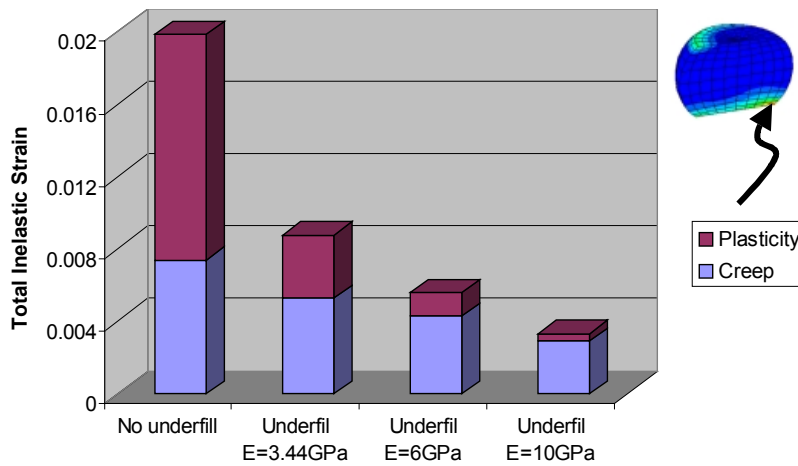
### ***-Underfill***

It is well known that underfill material improves flip chip package reliability by providing extra mechanical support to the solder joints. There are two major enhancing mechanisms. First, underfill can stiffen the package and reduce shearing in the solder

joint. Secondly, underfill can provide a hydrostatic stress state during its shrinkage at curing process. In this work, parametric modeling is used to evaluate the role of underfill in the power cycling samples. Figure 4.35 shows the equivalent plastic strain per cycle for the following cases: no underfill, and underfill materials with a Young's modulus of 3.44GPa, 6GPa, and 10GPa, respectively. The experimental specimens include non-underfilled samples as well as samples encapsulated by an underfill epoxy with a Young's modulus of 3.44GPa.



(a)



(b)

**Figure 4.35 Effects of underfill materials: (a) DAI and (b) CCB solder joint.**

This result shows that underfill has a greater effect on the CCB interconnect than on the DAI. It is shown that underfill significantly reduces plastic strain in both types of solder

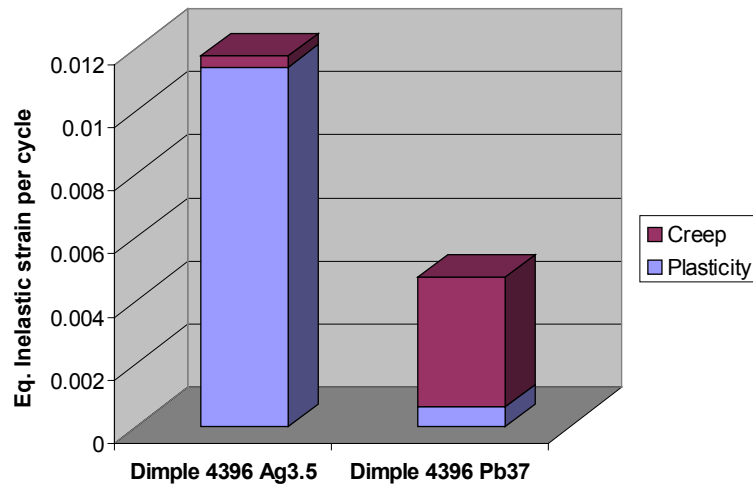
joints. The CCB joint without underfill material is much weaker than the non-underfilled dimple joints. Also, this result shows that the higher the Young's modulus for the underfill material, the less the inelastic strain range in the solder joints. Of course, since the underfill material is a type of epoxy and has a very special flow requirement, there is not much room left for engineering material stiffness and increasing the Young's modulus.

This study did not consider the nonlinear temperature effects of Young's modulus and adhesion strength between underfill epoxy with components. At temperatures below  $T_g$ , Young's modulus is high, and it decreases as the temperature increases. If the processing temperature goes beyond  $T_g$ , the underfill transforms from glassy to rubbery flow with a significantly lower Young's modulus, and finally behaves like a viscous flow (fluid) when the temperature increases further.

#### ***-Lead-free Ag3.5-Sn96.5 solder***

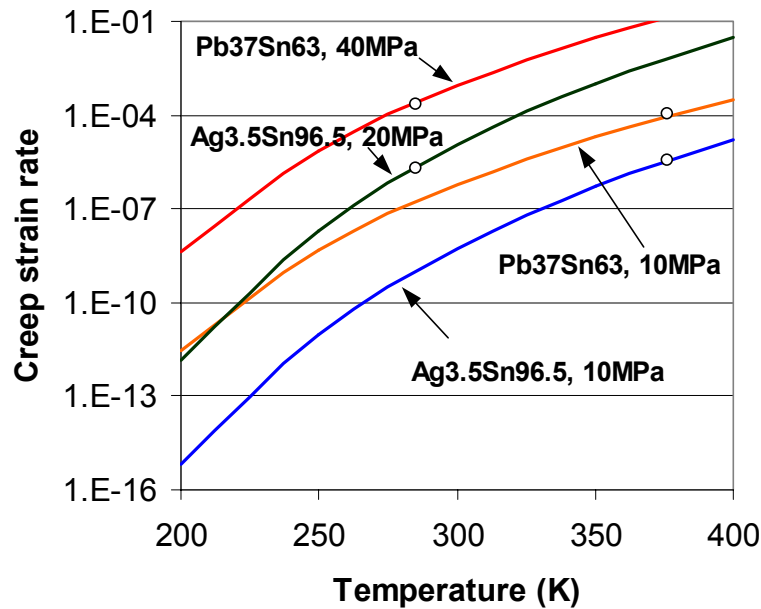
Environmental concerns have been raised as to the hazards of disposal of lead-containing electronic assemblies in the landfills, which can then be leached into underground water sources. A number of high-tin-based lead-free solders are under evaluation in industry to serve as alternatives to the eutectic tin-lead solder [165]. Furthermore, some research results show improvements in the fatigue resistance of lead-free solders under thermal and power cycling [151]. In this investigation, the eutectic tin-silver solder (Ag3.5-Sn96.5) has been evaluated.

Figure 4.36 shows the FEM-predicted equivalent creep and plastic strain per cycle (power cycling) for the weakest location in the Dimple Array joints, made using these two types of solders. This result indicates that the eutectic tin-silver solder does have a stronger creep resistance than the eutectic tin-lead solder. However, due to the fact that the eutectic tin-silver solder is soft (lower Young's modulus and lower yielding strength), it is more vulnerable to damage induced by the plastic deformation.



**Figure 4.36 FEM comparison of Ag3.5-Sn96.5 solder and Pb37-Sn63 solder under power cycling conditions.**

The physical explanation of the different creep resistances of Ag3.5-Sn96.5 solder and Pb37-Sn63 solder lies in their different plastic/creep properties. At high temperatures (100°C or more), both the eutectic tin-lead solder and the eutectic tin-silver solder have a yield strength of about 10MPa or lower. When the temperature decreases, the Pb37-Sn63 solder shows much higher yield strength than the Ag3.5-Sn96.5 solder. This indicates that at low-temperature stages during power/thermal cycling, the Pb37-Sn63 solder is more difficult to plastically deform and can thus sustain a higher stress level before yielding than the Ag3.5 solder. On the other hand, this high stress level in the eutectic Pb37-Sn63 solder promotes creep. Figure 4.37 shows a comparison of the creep strain rate of these two solders in their constrained format (i.e., in the form of solder joints) at 10°C and 100°C. For the eutectic Pb37-Sn63 solder joint, at 10°C the Mises stress is around 40MPa, and at T=100°C it is around 10MPa. For the lead-free Ag3.5-Sn96.5 solder joint, at 10°C the Mises stress is no more than 20MPa, and at 100°C the Mises stress is about 10MPa.



**Figure 4.37 Comparison of the creep strain rates of constrained solder (such as in the solder joint).**

At both low and high temperatures, the eutectic Ag3.5-Sn96.5 solder joint has a creep strain rate one to two orders of magnitude smaller than that of the eutectic Pb37-Sn63 solder joint, as shown in Figure 4.37.

A correlation between the FEM-predicted performance and the power cycling experiment has not been established due to limited Ag3.5-Sn96.5 samples.

***-Effects of dimple shapes***

Modeling results shown in Section 4.6 indicate that the center of the copper/solder interface may be a critical site due to high stress/strain concentration in that region. Therefore, a flat-bottom-configuration is modeled, in comparison to the original shape, as shown in Figure 4.38. The flat-bottom dimple has the same standoff height and diameter as those of the original dimple.

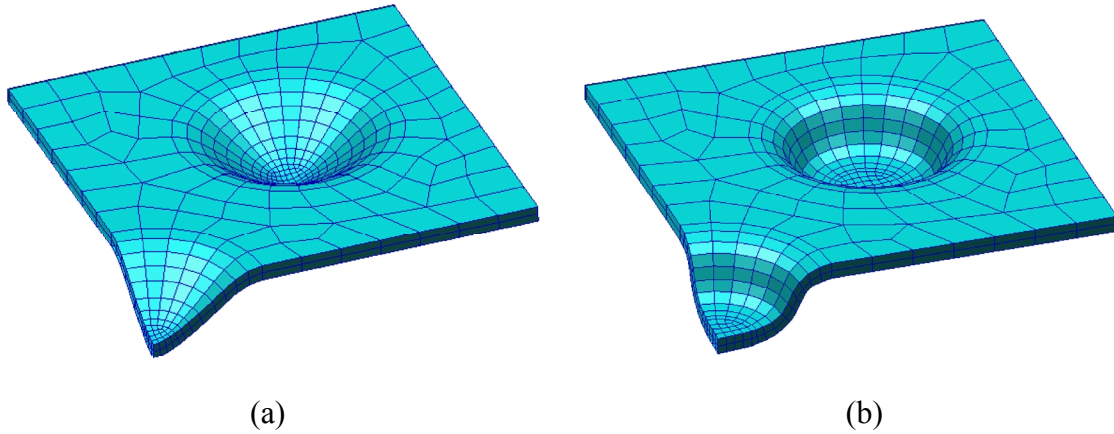


**Figure 4.38 Two dimple shapes: (a) the original and (b) a flat-bottom-dimple interconnect.**

Power cycling simulation shows similar stress contours for these two DAIs (Figure 4.39).

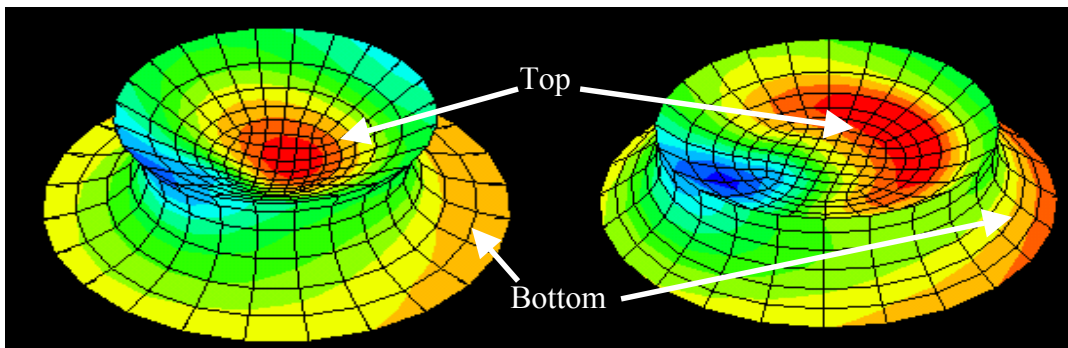


**Figure 4.39 Stress contours: (a) the original and (b) the flat-bottom-dimple solder joint.**

A comparison in the magnitude of the inelastic strain range between the two shapes is shown in Figure 4.40. The flat-bottom dimple has a smaller fatigue damage per cycle in the top region, while the bottom part of the solder joint has a slightly higher inelastic strain range. The change from the original to a flat-bottom-configuration does not seem to have a great impact on the reliability performance of the dimple solder joint.

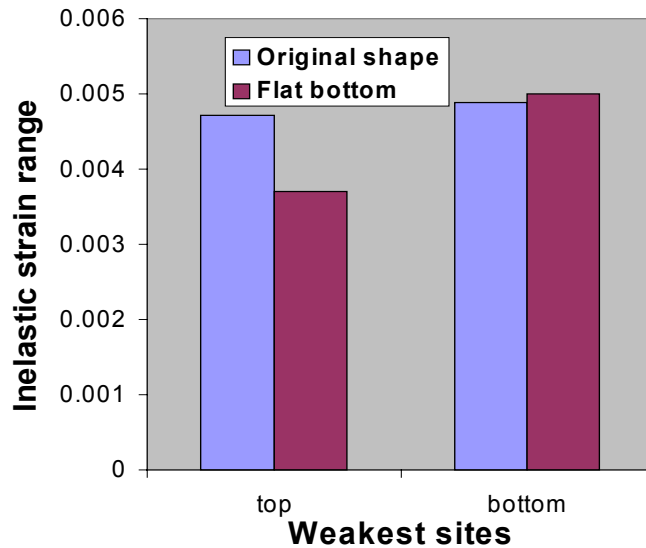


**Figure 4.40 Comparison of the inelastic strain range in the weakest sites of the original and the flat-bottom-shaped dimple solder joints.**

***-Discussion of the sources of modeling discrepancy***

FEM modeling offers a powerful tool for simulating material behavior under constrained conditions. However, a number of factors affect the accuracy of the modeling and lead to difficulty in validating of the numerical models.

a) Material models and sources of properties

Material models are chosen because they can describe the current dominant behavior of a specific material under given conditions. Therefore, it is an approximation of the real case. This selection also requires the person who does the modeling to have a good picture of material response. Furthermore, options provided in FEM codes are limited to the most general theories. For example, the model to describe solder thermoviscoplastic behavior used in this study assumes that the creep strain rate is independent from the plastic strain rate. It is convenient for FEM code to integrate these effects into linear algebraic equations, but it may not be absolutely correct.

Another big problem is the scattering of material property data from different references. It is not realistic to characterize each material used in this research. Therefore, material

constants and parameters are used because this set of data is thought to be most credible compared with other sets of data. Even if the most appropriate material data are used, simplification, and therefore errors, are still inevitable. For instance, solder creep data are tested under a certain strain rate. However, the strain rate can not be constant during thermal/power cycling.

#### b) Microstructures

The microstructure of material is often ignored because there is tremendous difficulty in incorporating this information into FEM modeling. Examples are the different microstructural characteristics of various solders, phase or grain-coarsening effects, and intermetallic compounds. Only a few research projects have tried to develop constitutive models for incorporating the effect of microstructural coarsening into FEM models [166] and none has led to a general approach to account for these effects.

### **Summary**

In this chapter, the Finite Element method has been extensively used to model the thermomechanical stresses/strains within the overall Dimple Array and CCB packages, as well as the thermoviscoplastic behavior of solder joints. Two sets of models were built for thermal and power cycling conditions. In this investigation, a constitutive theory was used to model the solder's total strain, which is assumed to be the sum of the elastic, plastic, and creep strains. The Prandtl-Reuss equations are used to describe the elastic-plastic behavior of solder. The steady-state creep was modeled using the Garofalo hyperbolic sine law.

FEM modeling results predict a five- to tenfold improvement in the thermal cycling reliability of the Dimple Array-type over the conventional CCB-type solder joint, while the thermal cycling experiment shows an improvement of eight- to more than tenfold in the Dimple Array solder joint. Furthermore, FEM shows higher normal stresses at the outer edge of solder/device interface in the CCB than are found in the dimple solder joint, which explains the early UBM delamination failures in the CCB samples.

FEM modeling results also predict a better power cycling reliability for the Dimple Array package, which was proved through metallographic cross-sectioning of samples at different testing stages. Underfill significantly improves CCB solder joint reliability, as also shown in FEM modeling. Furthermore, cracks initiated from the edge of the solder joints close to the device/solder interface and propagated to the center region, which is near the bottom of the copper dimple. These failure behaviors agree closely with the FEM modeling inelastic strain contours, proving that inelastic strain (creep and plasticity) is most likely the cause of the cracking.